



Universiteit Utrecht

Catchment-scale flood modeling using IMERG satellite based precipitation and WordView-2 imagery. A Case Study of Les Cayes, South coast of Haiti.

Master Thesis
in Earth Sciences

Constanza Maass Morales -MSc. Earth Surface and Water

Supervisors:
Steven de Jong (UU).
Victor Jetten (ITC).

Faculty of Geosciences
Utrecht University
July 2017

Acknowledgments

At first, I would like to thank dr. Steven de Jong and dr. Victor Jetten for supervising this research, which could not have been done without their guidance and support. I'm especially grateful to dr. Victor Jetten for introducing me with the project and facilitate the development of this research at the International Institute for Geo-Information Science and Earth Observation (ITC) of the University of Twente. In addition, I would like to thank dr. Francisco Zambrano from Universidad de Concepción for his continued help and orientation during the rainfall analysis.

I extend my gratitude to Raha Hakimdavar from Columbia University for providing the rain-gauge data used in this study. In addition, I would like to thank DigitalGlobe Foundation for providing me with multispectral and high spatial resolution images through an imagery grant.

I would also like to thank the National Commission for Scientific and Technological Research in Chile (CONICYT-CHILE), who provided me with a scholarship to fund my MSc studies at Utrecht University.

And last, but not least, I would also like to thank my partner Felipe Lobos Roco and my family and friends, for their encouragement and moral support throughout these past 5 months.

Catchment-scale flood modeling using IMERG satellite-based precipitation and WordView-2 imagery. A Case Study of Les Cayes, South coast of Haiti.

Abstract. The Hurricane Matthew was one of the most recent catastrophic events to impact the Caribbean, the Bahamas, and the Southeastern United States in October of 2016. In Haiti, the powerful winds and heavy rainfall caused storm surges and major flooding through the entire country, devastating the western edge and the south coast of Haiti. Considering the tremendous lack of hydrometeorological data in the country and the high cost and institutional capacity needed to collect and manage field measurement; this study investigated the use and usefulness of remote sensing data for integrated flood modeling at a catchment scale in the South region of Haiti.

In particular, the study evaluated the suitability of the use of Integrated Multi-satellitE Retrievals for GPM (IMERG) product, to estimate extreme rain events in the South region of Haiti. Secondly, the research investigated the possibility of using multispectral and high-resolution optical images, to delineate the extent of the Matthe flood episode occurred in the catchment of Les Cayes. Furthermore, the study tested the potential of IMERG satellite product and WordView-2 images as sources of information for simulate the flooding episode and calibrate the modeling.

I.	INTRODUCTION	5
1.1.	RESEARCH PROBLEM.....	5
1.1.1	IMPORTANCE AND SIGNIFICANCE	6
1.1.2	RESEARCH CHALLENGE	6
1.2.	RESEARCH QUESTIONS.....	7
1.3.	BACKGROUND	8
1.3.1.	STUDY AREA.....	8
1.3.2.	HURRICANE MATTHEW.....	9
II.	METHODOLOGY	11
2.1.	RAINFALL ESTIMATION EVALUATION.....	11
2.1.1.	DATASET.....	12
2.1.2.	DATA COMPARISON.....	13
2.2.	FLOOD EXTENT DELINEATION	15
2.2.1.	DATASET.....	16
2.2.2.	IMAGE PRE-PROCESSING	16
2.2.3.	PRE-AND-POST- EVENT LAND USE MAPPING	17
2.2.4.	LAND USE CHANGE DETECTION	19
2.3.	FLASH FLOOD MODELING	19
2.3.1.	LISEM MODEL	20
2.3.2.	MODEL DATASET.....	23
2.3.3.	FLASH FLOOD SIMULATION AND CALIBRATION	24
III.	RESULTS: RAINFALL ESTIMATION EVALUATION.....	25
3.3.	EXPLORATORY ANALYSIS OF JOAQUIN RAIN EVENT	25
3.4.	STATISTICAL EVALUATION.....	26
3.4.1.	HOURLY RAIN INTENSITY COMPARISON.....	26
3.4.2.	RAIN INTENSITY COMPARISON AT DIFFERENT TIME-SCALES	28
IV.	RESULTS: FLOOD EXTENT DELINEATION	31
V.	RESULTS: FLASH FLOOD SIMULATION OF MATTHEW RAIN EVENT	33
5.1.	CALIBRATION RESULTS	33
5.2.	SIMULATED AND OBSERVED FLOODED AREA COMPARISON	35
5.3.	HYDROLOGICAL RESPONSE AND FLOOD CHARACTERISTICS OF MATTHEW EVENT	37
VI.	DISCUSSION.....	40
VII.	REFERENCES	44
VIII.	APPENDIX	48

I. INTRODUCTION

1.1. RESEARCH PROBLEM

The Caribbean island of Hispaniola, territory shared by Haiti and the Dominican Republic, is in a tropical zone prone to extreme flood events, where the scarcity of hydrometeorological makes any flood studies challenging and in some cases not possible.

Located in the path of tropical storms and hurricanes, Hispaniola Island is frequently exposed to flash floods episodes produced by intense precipitations within a relatively short period of time. Historically, severe flood events have recurrently affected the island causing thousands of casualties, people displacement, economic losses, environmental damages and sanitary emergencies (Brandimarte *et al.*, 2009; Bozza *et al.*, 2016). The extremeness of the rain events that seasonally hit the island, these natural disasters are a result of the weather phenomena combined with a highly vulnerable territory. Haiti, rated as the poorest country in the western hemisphere, has shown to be particularly vulnerable to these natural hazards. Only in the last decade, five floods episodes derived from heavy hurricanes rains, have recurrently devastated the country (Ike, 2008; Gustav, 2008; Sandy, 2012; Joaquin, 2015; Matthew, 2016). The low resistance and resilience of the country to floods have been related to a sum of factors in the literature: the social composition of the population, 80% of Haiti's populations live under the poverty line (CU, 2017), the unplanned urban expansion on river floodplains (CU, 2017); the weakness of the urban infrastructure and the intense processes of deforestation, since 1986 the forest coverage has decreased a 70% (Dolisca *et al.*, 2007).

It may be possible to realize flood mitigation measures in the coastal zones and upstream catchments, but for that, the flood dynamics in relation to the exposure of people, houses, and infrastructure, need to be better understood. Several methods are available to study and simulate floods, which are needed to setup hazard and flood risk assessment, floodproofing strategies and flood forecasting and early warning emergency plans (Hall and Solomantine, 2008; Bozza, et al., 2016). The approaches range from empirical methods based on in situ flood observations combined with remote sensing data or weighted combination of flood-related GIS layers; to dynamic methods based on integrated catchment modeling (Jetten and Chavarro, 2016). Given the fact that flooding is an extremely complex process subject to change, modeling methods need a large amount of data with high spatial and temporal resolution (e.g rain intensity, river discharge, elevations, land uses, among others). However, a good dataset does not guarantee a good or realistic flood estimation. Therefore, the calibration of the model is essential to ensure that it accurately represents the system being simulated.

Haiti is considered one of the most data scarce countries in the Caribbean (CU, 2017). The lack of institutional capacity for collecting and managing hydrometeorological data in a central database, resulted in scattered data sets from different monitoring programs, which are often lost or discontinued over time. Concerning rainfall measurements, the Global Historical Climatology Network (CHCN) has 93 weather stations in Hispaniola island, from which 10 are located in Haiti and only one in the South Department, where hurricanes tend to make landfall first. About river discharge data, even though some historical data is available for the period 1922 - 1940 and the late 1980s, no systematic streamflow

monitoring program has ever existed in Haiti (CU, 2017). Recently, a joint project between United Nations Environment Programme (UNEP), the Government of Haiti (GoH) and Columbia University (CU) was developed to investigate the hydropower potential in the South Department of Haiti. As part of the project, a hydro-meteorological monitoring network (HEN) that included weather stations and streamflow measurements, was implemented by Columbia University. In particular, 11 weather stations were installed across the southwestern coast of Haiti during the period 2010-2014. Although the hourly weather data was publicly available on the internet until the year 2016, the current state of the stations is unknown. From the existing measurement period, there are some cases where the stations have stopped working, probably due to the extreme weather conditions or lack of means for maintenance.

Recently, satellite-based rainfall estimates (SRE) products provide an unprecedented opportunity for a wide range of hydrological studies, where ground meteorological data is missing. Evaluations of different SRE products with ground data observations have shown the potential of using rainfall remote sensing data at regional scale studies (Zambrano *et al.*, 2017; Zambrano-Bigiarini *et al.*, 2017). Although the resolutions of the current products are still considered coarse for catchment-scale studies in Haiti (where important rainfall variability have been found) (CU, 2017), the new SRE product from NASA with half hourly data at a grid of 0.1°, provide a new alternative for a data-scarce country like Haiti. Similarly, flood extent maps derived from multispectral and high-resolution satellite images has emerged as an alternative to discharge data and flood extent in situ observations, for calibrating and evaluating hydrological and hydraulic flood models (Di Baldassarre, Schumann and Bates, 2009).

1.1.1 IMPORTANCE AND SIGNIFICANCE

Considering the tremendous lack of hydrometeorological data in Haiti, the high cost and institutional capacity needed to collect and manage field measurement; this study will investigate the use and usefulness of remote sensing data for integrated flood modeling at a catchment scale in the South region of the country.

In particular, the study attempts to evaluate -for the first time- the suitability of the use of Integrated Multi-satellitE Retrievals for GPM (IMERG) product, to estimate extreme rain events in the South region of Haiti. Secondly, the research aims to investigate the possibility of using pre and post event multispectral Worldview-2 images, to delineate the extent of the flood episode occurred during the pass of Matthew Hurricane in the city of Les Cayes. Furthermore, the study will test the potential of IMERG satellite product and WordView-2 images as sources of information for simulate the flooding episode and calibrate the modeling.

Summarizing, this study aims at increasing our knowledge about the suitability of using IMERG satellite product and WordView-2 images in flood modeling, as a cost-effective complement to ground-based measurement in Haiti and in similarly data-scarce regions. Moreover, flood simulations can be incorporated in flood hazard studies which formed the basis for flood risk management.

1.1.2 RESEARCH CHALLENGE

Investigating the possibility of developing a good or realistic flood study based upon hydrological and hydraulic modeling in Haiti, with almost a complete lack of ground hydro-meteorological data is the main challenge of the research.

On one hand, there is a unique opportunity to determine the accuracy of an extreme rain event estimation derived from the IMERG product, with hourly meteorological data derived from the HEN meteorological network. However, the effective time period to make the comparison is limited to the data availability. The IMERG data is only available from March of 2015 to the present, while the ground meteorological data varies between 2011 and the first months of 2016. Given the fact that there is no available ground data of Mathew event (October 2016), the first challenge is to find and evaluate another extreme rain event that has occurred during 2015.

On the other hand, the availability of WorldView-2 satellite images before and after the Matthew flood event, which has a high spectral and spatial resolution, is also a unique opportunity to delineate the flood extent and calibrate the flood modeling. Given the fact that flood water surface is not visible in the post-event images (probably because these were captured five and six days after the event), the method for estimating the flood extent is another challenging step of the study.

1.2. RESEARCH QUESTIONS

The main questions and sub-questions that are investigated in this MSc thesis are:

How accurate can the Matthew flood episode be modeled in Les Caye's catchment, with a poor availability of ground-hydrometeorological data in Haiti?

- How accurate can we assess precipitation of an extreme rain event from satellite-based IMERG products?
- Can the extent area of the flood episode be detected from satellite images, if the inundation surface is not present in the post-event imagery?
- Is the combination of input data and model parametrization capable of simulating the detected flood extent?

1.3. BACKGROUND

The research area selected in this study was proposed by the International Institute for Geo-Information Science and Earth Observation (ITC) of the University of Twente, in the light of a collaboration project with the Red Cross. The purpose was to provide more understanding of the runoff and flooding processes of the Southern Department of Haiti, where since 2016 the Red Cross Princess Margriet Foundation has a flood mitigation project to protect settlements and agriculture areas (Rode Kruis Prinses Margriet Fonds, 2016).

1.3.1. STUDY AREA

The study area is located in the southwest of the Republic of Haiti, which belongs to the western part of the Hispaniola island in the Caribbean Greater Antilles archipelago. Haiti occupied the third part of the island, which shares with the Dominican Republic.

As is shown in Figure 1 the research area is located in the southwest catchment of Les Cayes, which belongs to the South Department communes of Camp Perrin, Les Cayes, Torbeck, and Chantal. The catchment covers a total area of 268.25 km². Ravine du Sud River is the main fluvial course, which runs from the peak of Macaya (2,361 meters above sea level) to the Peninsula of Tiburon at the Caribbean Sea.



Figure 1. Location of the study area in South-west Haiti.

The northwest zone of the catchment is a mountainous area partly situated in the Macaya National forest reserve. The elevation profile of the catchment (Figure 2) shows that 23% of the catchment's area is above 500 meters, while less than 12% of the catchment's area has greater than 1,000 meters (CU, 2017). In terms of land use, half of the catchment is covered by moderate to dense agriculture land units, with agroforestry 11% of the area, savannah 8% and forest 7% (CU, 2017).

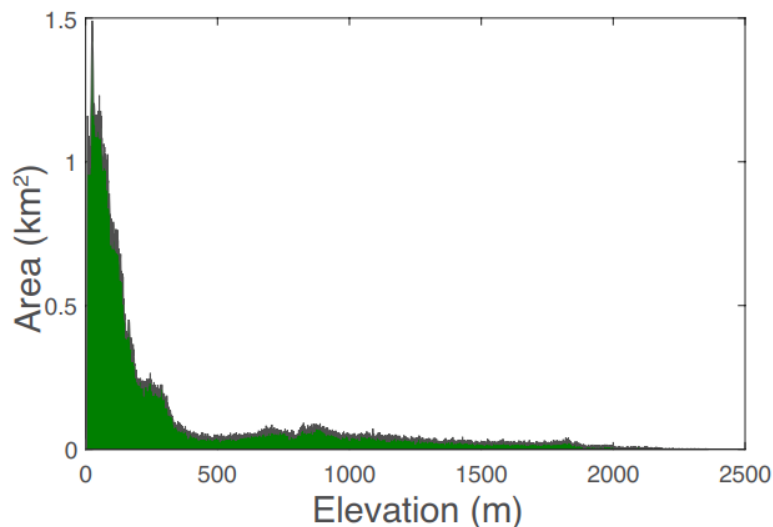


Figure 2. Elevation profile of the study area, from CU (2017)

1.3.2. HURRICANE MATTHEW

The flood event investigated in this study was triggered by the intense precipitations generated from the passage of Hurricane Matthew in Haiti. The Hurricane Matthew was one of the most recent catastrophic rain events to impact the Caribbean, the Bahamas, and the Southeastern United States in October of 2016. The hurricane began as a tropical wave off the coast of Africa in late September 2016 and became a tropical storm as it moved westward across the Atlantic Ocean just north of the South America coast (Weaver *et al.*, 2016). The system strengthened into a hurricane on September 29, reaching a peak intensity on October 1st with maximum winds of 260 kilometers per hour, classifying as a Category 5 storm on the Saffir-Simpson scale (Weaver *et al.*, 2016). The path followed by the Hurricane is shown in Figure 3.

In the case of Haiti, the hurricane made landfall on October 4th as a Category 4 storm, with winds of up to 233 kilometers per hour and rainfall estimation over 500 mm in 24 hours (Pacific Disaster Center, 2016). The powerful winds and heavy rainfall caused storm surges and major flooding through the entire country, devastating the western edge and the south coast of Haiti (Relief Web, 2016). Although the official number of people killed by the storm in Haiti is 576 (République d'Haïti, 2016), other sources raised the estimation up to 1,000 people (CBS NEWS, 2016; REUTERS, 2016). According to the Haitian government, the World Bank and the Inter-American Development Bank (IADB), the estimate damages and economic losses reached to USD \$1.89 billion or 22% of the GDP (CEDIM, 2016). In the South department of Haiti, the port-city of Les Cayes was seriously affected by floods. Local news reported that the streets were impassable because of flooding, landslides or fallen trees and that the water was shoulder high in parts of the city (CBS NEWS, 2016).

According to the Meteorology Institute of Cuba (INSMET, 2016), the rainfall registered during Matthew event in the province of Guantanamo (southeast of Cuba) was spatially variable. The values registered by four meteorological stations are shown in Table 1. The highest values were registered by a station located at the East end of the island (P. de Maisí), with a total accumulative rainfall of 661.3 mm (October 4-5) and a maximum rainfall in 24 hours of 542.4 mm.

The USGS (Weaver, Feaster and Robbins, 2016) reported that the total accumulative rainfall of the event recorded during October 7-9 by a meteorological station (ID: 02105500) in North Carolina (southeast of US) was 428.498 mm. In addition, the maximum total rainfall accumulated per different time periods were observed on October 8th: 2 hours (135 mm), 3 hours (179 mm), 6 hours (269 mm), 12 hours (383 mm), 24 hours (419 mm). The return periods of observed maximum totals rainfall correspond to intensities at or exceeding 200 years: 2 hours (at 200 years), 3 hours (between 500 and 1,000 years), 6 hours (>1,000 years), 12 hours (>1,000 years), and 24 hours (>1,000 years).

Table 1. Accumulative rainfall of Matthew event in Cuba (mm), from INSMET (2016)

Meteorological Stations	Total during event (4 th -5 th October)	Maximum in 24 hours (4 th October)
P de Maisí	542.4	661.3
Jamal	174.3	191.9
Caujerí	213.9	400.0
Palenque de Yateras	221.5	377.7

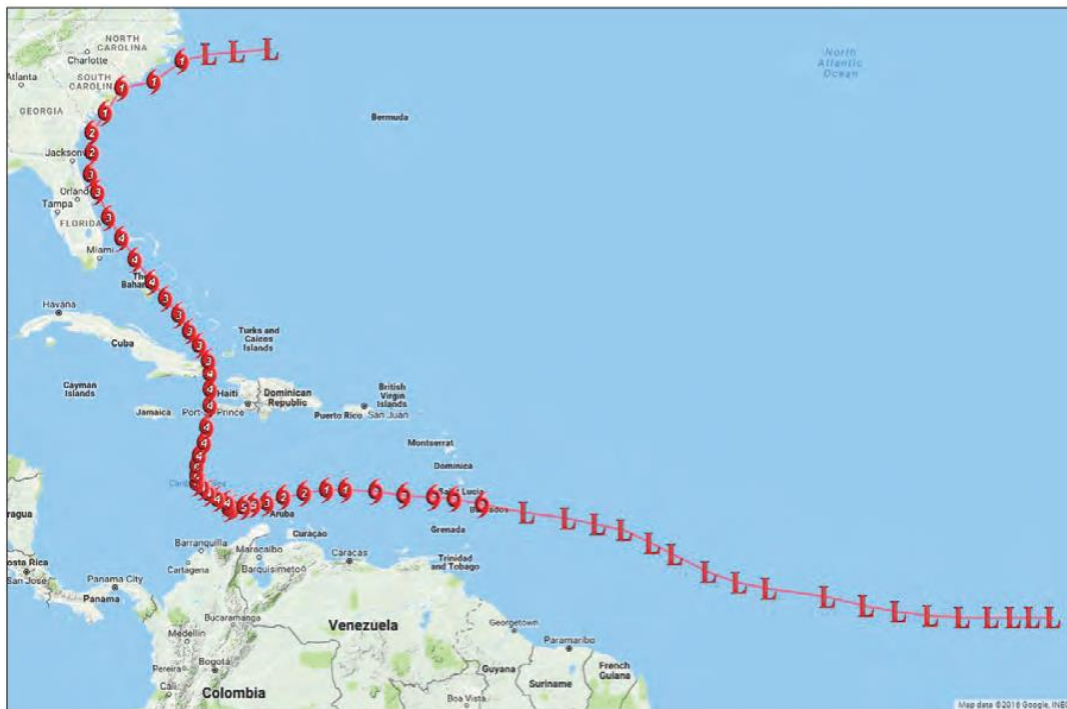


Figure 3. Track of Hurricane Matthew through the Atlantic basin from September 29 to October 9, 2016 (Weaver et al., 2016). Letter “L” indicates a low-pressure system with a counter-clockwise direction.

II. METHODOLOGY

This chapter describes the research method applied in this study, which was developed through three consecutive phases. The first one refers to the analysis of the accuracy of IMERG satellite-based rainfall product with ground data. As no rain gauge data from Matthew event was available in the study area, the rain event derived from the pass of Joaquin Hurricane in the South of Haiti was analyzed in the first phase. The second phase refers to the flood extent delineation on the basis of satellite images, of the flooding episode occurred during the pass of Hurricane Matthew in Les Cayes. The last stage refers to the simulation of the flood episode and the validation of the results. Figure 4 shows a diagram of the general strategy followed, where phases one and two yields the necessary input for phase 3.

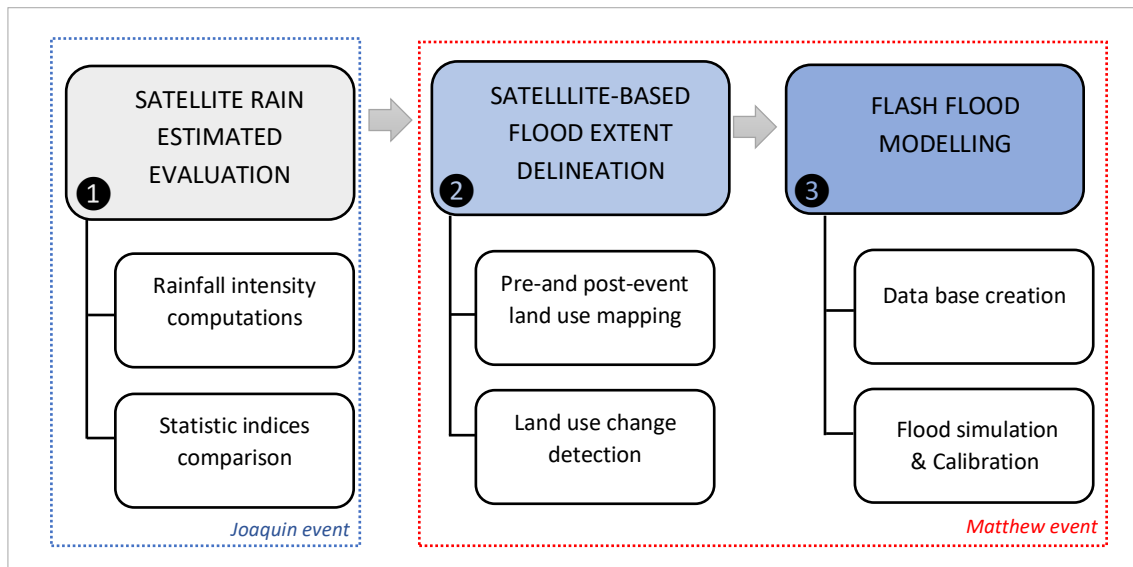


Figure 4. Methodology Flowchart

2.1. RAINFALL ESTIMATION EVALUATION

The key triggering factor for flash floods generation is large volumes of high-intensity precipitations in a brief period of time. In this regard, an extreme rain event was defined in this study in terms of daily accumulated rain based on the criteria suggested by Zambrano *et al.*, (2017). Specifically, as shown in Table 2, a rain episode with intensities greater than 40 mm/day will be characterized as an extreme rain event.

Table 2. Classification of rainfall events severity based on its daily intensity. Modified from (Zambrano et al., 2017)

Severity of the event	Daily Intensity Class	Intensity (i), [mm d ⁻¹]
Non-extreme event	No Rain	0 - 1
	Light rain	1- 5
	Moderate rain	5 - 20
	Heavy rain	20- 40
Extreme event	Violent rain	≥ 40

Based on the availability of rainfall data of an extreme rain event in the South of Haiti, the analyzed rain episode was Joaquin Hurricane which was formed one year before Matthew Hurricane. Joaquin reached its peak rainfall intensity in the Bahamas at October 2nd (to the north of Hispaniola island, see Figure 3), triggering river flooding and landslides in the northwestern part of Haiti (Berg, 2016). Even though the selected rainfall episode was less intensive than Matthew over the South-West of Haiti, intensities higher than 40 mm d-1 were registered in all the rain gauge stations evaluated for Joaquin.

2.1.1. DATASET

Rain gauges data

Hourly rainfall data were obtained from six meteorological stations installed in the South Department of Haiti by Columbia University (details of the weather network can be found in chapter I, section 1.1). The low number of stations that could be used in this analysis illustrates the lack of hourly rainfall records from in situ gauges that are available in Haiti. The location and main characteristics of the stations are shown in Figure 5 and Table 3, respectively.

Table 3. Overview of the weather station used in the study

Station name	Station ID	Latitude	Longitude	Altitude (masl)	Location reference
Tiburon	TIB	18.32	-74.4	14	City of Tiburon
Port a Piment	PPMT	18.26	-74.1	24	City of Port a Piment
Ravine du Sud	RDS	18.38	-73.89	335	4 km NW from Camp-Perrin City
Saut Mathurine Dam	SMD	18.37	-73.86	323	1.5 km upstream from of LSM
Lower Saut Mathurine	LSM	18.37	-73.84	212	5 km NE from Camp-Perrin City
Upper Saut Mathurine	USM	18.39	-73.86	860	7 km NE from Camp-Perrin City

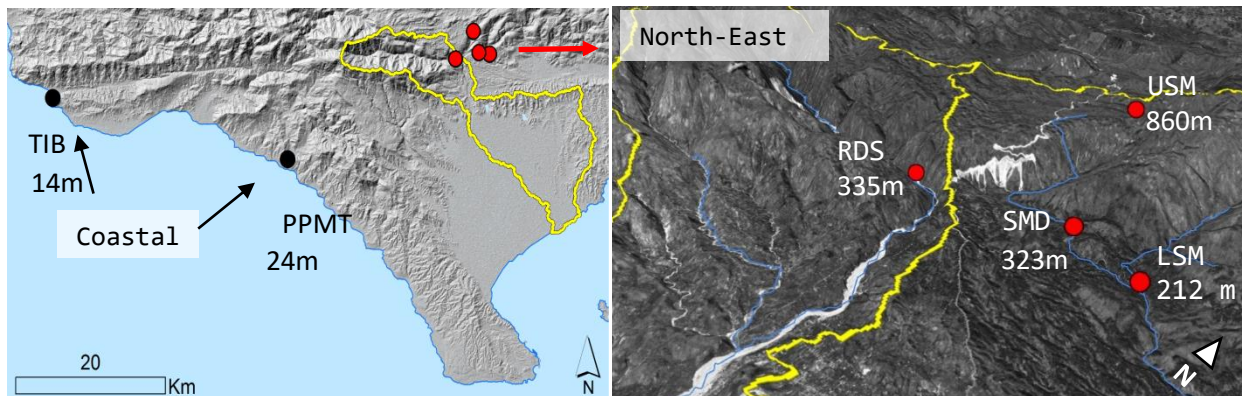


Figure 5. Location of the rain gauge stations used in the study. Black dots represent the coastal stations and red dots, the stations located at the north-east of the study area.

Rainfall satellite-based data

The “Late Run” of the Integrated Multi-SatellitE Retrievals for GPM Level-3 product (IMERG-L v.03.) was used to estimate the rainfall intensities of the study. The SRE is currently available since March 2015 and can be freely downloaded from the NASA website. It has a spatial resolution of $0.1^\circ \times 0.1^\circ$ and is available at several time scales such as half-hourly, 3-hourly and daily. IMERG estimates the precipitation combining data from all passive microwave sensors of the GPM satellite constellation, which is finally intercalibrated, merged, and interpolated using the Goddard Profiling Algorithm (Huffman *et al.*, 2013). In particular, the

IMERG “Late” version is a product which is run 16 hours after the real time, with slight calibration (Huffman *et al.*, 2015). The data used in this study were half-hourly data, which were converted to hourly rain intensities values. The main characteristics of the SRE are summarized in Table 4.

Table 4. Characteristics of the IMERG-L V.03 satellite-based product used in the study

Dataset	Full name	Temporal Resolution	Spatial Resolution	Begin Date	Reference
IMERG-L v03.	Multi-satellite Retrievals for GPM, Level 3, Late run.	Half Hourly	0.1° (10.5 km)	March 2015-present	(Huffman <i>et al.</i> , 2015)

2.1.2. DATA COMPARISON

Statistical indices

A pairwise comparison was performed to compare the rain ground data observations to the corresponding SRE pixel (point-to-pixel), as suggested by recent precipitation products assessment (Dembélé and Zwart, 2016; Wang *et al.*, 2017; Zambrano *et al.*, 2017; Zambrano-Bigiarini *et al.*, 2017). Figure 6, shows the locations of the six rain gauge stations and the corresponding pixels. Four stations (USM, LSM, SMD, RDS) falls at the same pixel of the SRE, therefore were compared with the same estimated values.

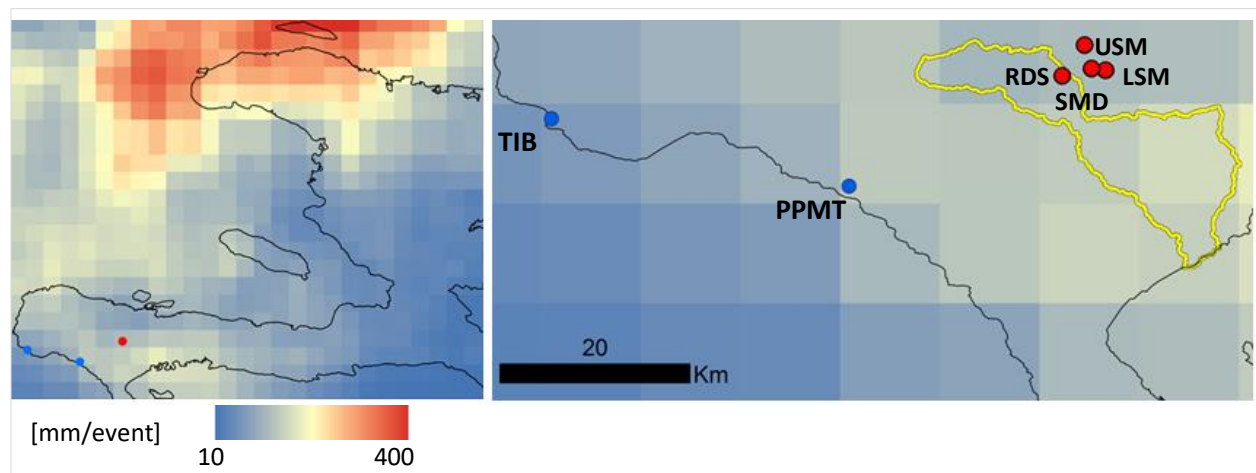


Figure 6. Location of rain gauge stations against the SRE pixels of 10.5 km X 10.5 km. The left image shows the total accumulated rainfall of Joaquin event in Haiti and the right image zooms into the study area.

Six statistical indices were selected to quantitatively evaluate the accuracy and error of the IMERG-L product estimating the amount of rainfall of Joaquin event. The statistics were computed using the hourly rain intensities values and cumulative rainfall values at different time scales (1, 3, 6, 12 hours). The evaluation time was conducted from 29th September 19:00 to 3rd October 18:00, of the year 2015.

The main specifications of the used statistical indicators are summarized in Table 5 and described below:

- 1) Pearson correlation coefficient (r): Measure of the linear correlation between the observations and satellite values (Eq.1, Table 5). The values can range from +1 (perfect positive correlation) to -1

(perfect negative correlation), with zero indicating the absence of linear correlation. The main risk of this indicator is its inability to detect changes in location and scale between the two variables.

- 2) Mean Error (ME): Average difference between the estimated and the observed rainfall values (Eq.2, Table 5). Express the average estimate error in units of the variable of interest, where a positive ME shows that the estimated values are overestimated, while a negative sign shows it is underestimated. The values can range from minus infinity to infinity, being 0 the optimum value for a perfect match. The main risk of this indicator is that large positive and negative differences can cancel each other out, producing an ME near "0", even though there is not a perfect match.
- 3) Mean Absolute Percentage Error (MAPE): Average of the absolute differences between the estimated and the observed rainfall values, divided by the mean of the observed values (Eq.3, Table 5). Measures the average magnitude of the errors in percentages, without considering their direction. The values can range from zero to infinity, being 0 the optimum value for a perfect match.
- 4) Root Mean Square Error (RMSE). The square root of the average of squared differences between estimated and observed rainfall values (Eq.4, Table 5). As ME the RMSE measures the average magnitude of the estimate errors in units of the variable of interest, but since the difference are squared before they are averaged, the RMSE gives a relatively high weight to large errors. The values can range from zero to infinity, being 0 the optimum value for a perfect match.
- 5) Multiplicative BIAS (BIAS): Sum of estimated values divided by the sum of observed values (Eq.5, Table 5). Reflects the number of times to which the estimated rainfall values is over- or under the observed values. The values can range from zero to infinity, being 1 the optimum value for a perfect match.
- 6) Efficiency score (EFF). (Eq.6, Table 5). Express the skill of the estimates rainfall values relative to the mean of the observed values. A negative EFF shows that the observed mean is better than the estimate, an EFF of zero shows that the observed mean is as good the estimated mean, and a positive EFF shows a good skill. The values can range from minus infinity to 1, being 1 the optimum value for a perfect match.

Table 5. Statistics used to compare in situ rain gauge measurements and the estimates from the IMERG-L satellite product (Zambrano-Bigiarini *et al.*, 2017). Number of pairwise observations(N), rain gauge observation (G), estimated precipitation value (S), mean of the rain gauge observations (\bar{G}), mean of the estimated precipitation values (\bar{S}).

Statistical indicator	Equation Number	Formula	Unit	Values range	Optimum value
r	(1)	$r = \frac{\sum(G - \bar{G})(S - \bar{S})}{\sqrt{\sum(G - \bar{G})^2} \sqrt{\sum(S - \bar{S})^2}}$	-	-1 to 1	1
ME	(2)	$ME = \frac{1}{N} \sum (S - G)$	mm	$-\infty$ to ∞	0
MAPE	(3)	$MAPE = \frac{100}{\bar{G}} \sum \frac{ S - G }{N}$	%	0 to ∞	0
RMSE	(4)	$RMSE = \sqrt{\frac{1}{N} \sum (S - G)^2}$	mm	0 to ∞	0
BIAS	(5)	$BIAS = \frac{\sum S}{\sum G}$	-	0 to ∞	1
E_{FF}	(6)	$Eff = 1 - \frac{\sum(S - G)^2}{\sum(G - \bar{G})^2}$	-	$-\infty$ to 1	1

2.2. FLOOD EXTENT DELINEATION

The extent of the Matthew flood episode in Les Caye's catchment detected from pre-and post-event satellite imagery, is used in this study to validate the flooding area simulated by the model LISEM. The proposed procedure to derive the satellite-based flood extent map is shown in Figure 7 and explained in the following sections.

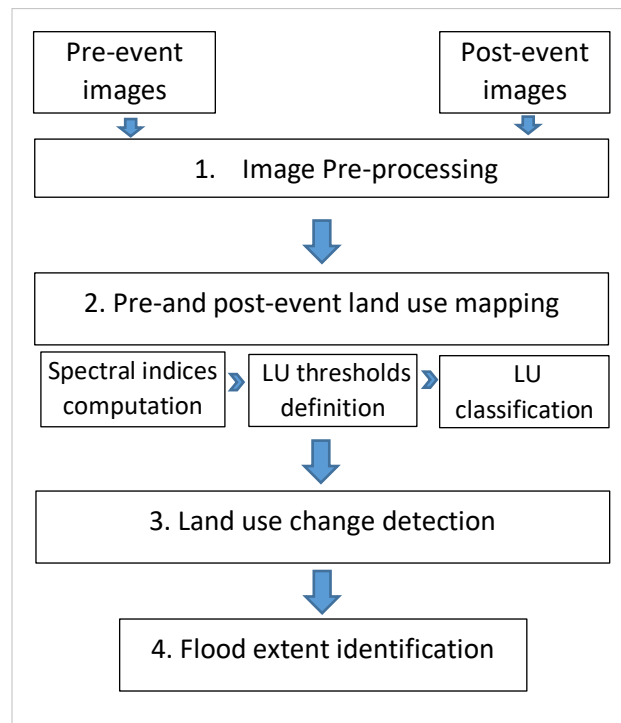


Figure 7. Flow chart of the satellite-based flooding extent delineation method.

2.2.1. DATASET

Two types of satellite sensors were used to assess the event flooding extent, WordView-2 (WV-2) and GeoEye-1 (GE-1). The imagery was provided by Digital Globe Foundation and consisted of multispectral and high spatial resolution products. The images acquired were Standard Imagery Products, which already has radiometric, sensor and geometric corrections. The spectral and spatial characteristics of both images are shown in Table 6.

Table 6. Characteristics of WordView-2 and GeoEye-1 images

Satellite Images	Spectral Band	Spectral Range(nm)	Spatial resolution (m)
WordView-2	Panchromatic (PAN)	450 - 800	0.5
	Coastal Blue	400 - 450	2.0
	Blue	450 - 510	2.0
	Green	510 - 580	2.0
	Yellow	585 - 625	2.0
	Red	630 - 690	2.0
	Red Edge	705 - 745	2.0
	Near-infrared 1 (NIR-1)	770 - 895	2.0
	Near-infrared 2 (NIR-2)	860 - 1040	2.0
GeoEye-1	Panchromatic (PAN)	450 - 800	0.5
	Blue	450 - 510	2.0
	Green	510 - 580	2.0
	Red	655 - 690	2.0
	Near-infrared 1 (NIR-1)	780 - 920	2.0

The images were captured before and after the Hurricane Matthew event, which made landfall in Haiti on 4th October 2016. The specifications of the images used to perform the flood extent delineation are shown in Table 7.

Table 7. Specifications of images used in the study

Date	Satellite Image	Period	Cloud Cover	Watershed Cover
5-01-2013	WordView-2	pre-event	5%	Medium and lower part
1-10-2016	WordView-2	pre-event	39.2%	Lower part
8-10-2016	GeoEye-1	post-event	0.1%	Lower part
9-10-2016	WordView-2	post-event	14.6%	Medium and lower part

2.2.2. IMAGE PRE-PROCESSING

In order to prepare the images for the further analysis, two steps were performed (using the software ENVI version 5.2):

First, the raw pixel values or digital numbers (DN) were converted to top-of-atmosphere (TOA) reflectance values (0 to 1.0), according to Equation 7 (Updike and Comp, 2010):

$$P_{\lambda} = \frac{\pi L_{\lambda} d^2}{ESUN_{\lambda} \sin \theta} \quad \text{Equation 7}$$

Where:

L_{λ} =Radiance in units of W/(m²*sr*μm).

d = Earth-sun distance, in astronomical units.

$ESUN_{\lambda}$ =Solar irradiance in units of W/(m²*μm).

θ =Sun elevation in degrees.

The process was performed through the Radiometric Calibration function, for each scene. The gains, offsets, solar irradiance, sun elevation, and acquisition time values were obtained directly from the metadata of the images.

Secondly, the scenes with the multispectral bands of each date were assembling using the mosaicking function (resampling method nearest neighbor). The final extent of the images after the mosaicking is shown in Figure 8. The pre-and post-event images covered the medium and lower part of Les Caye's catchment, and therefore the flood extent delineation was performed in this region.

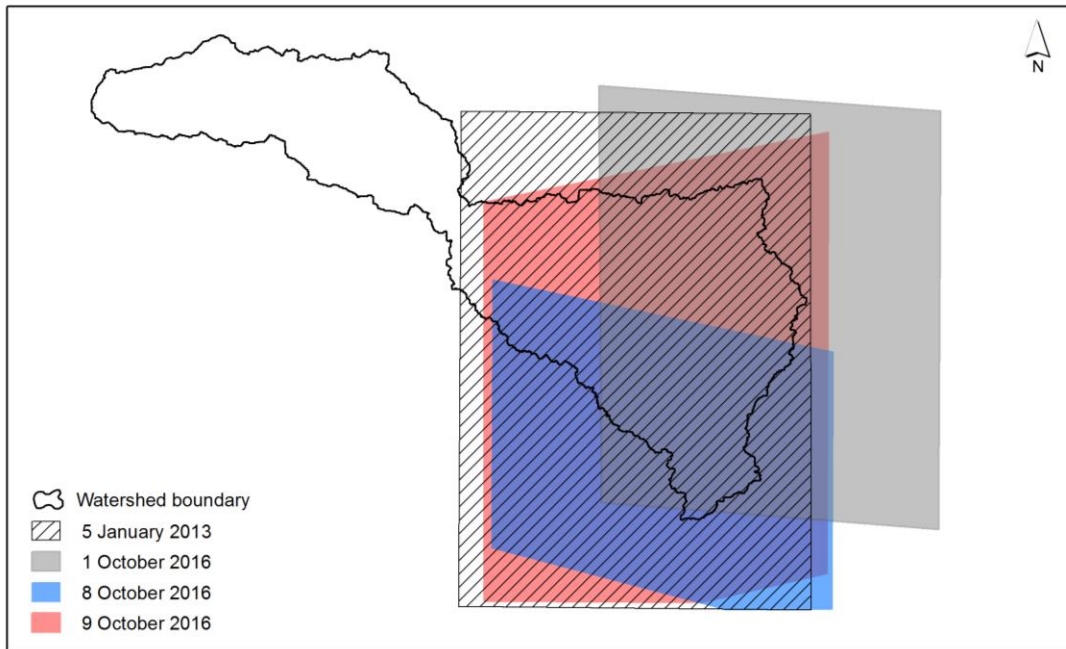


Figure 8.Section of the images covering the study area

2.2.3. PRE-AND-POST- EVENT LAND USE MAPPING

As the flood water surface was not visible on the available post-event satellite images, land use changes were explored to assess the flood extent of Matthew event in Les Caye's catchment.

High-resolution land-use maps were reconstructed for the area after and before the event, in order to first visualize changes in vegetation, water surface, bare soil and impervious land units (roads, parking lots, urban areas, etc.). The WV-2 and GE-1 images were investigated under six different spectral indices to establish an effective land mapping, were finally three were selected to fund the land unit classification: Normalized Difference Vegetation Index (NDVI), Normalized Difference Water Index (NDWI) and Road Extraction Index (REI). The NDVI and NDWI were used to identify vegetation cover and surface water, respectively. The indices were computed through variations of the original ratios, that were proposed by Malinowski *et al.* (2015) and Wolf (2012), based on the available spectral bands of WV-2 images. The REI index was developed by Shahi *et al.* (2015) to extract asphalt road networks from WV-2 images. However, it was used to detect bare soils and impervious surfaces (asphalt roads and build up areas). The thresholds values set to identify each class were defined by trial and error. The specifications of the indices are shown in Table 8.

Table 8. List of the multispectral indices used for the land use classification of WV-2 and GE-1 images.

Index	Formula	References	Application
NDVI	$NDVI_0 = NIR - Red/NIR + Red$	Tucker (1979)	original index
	$NDVI_1 = NIR_1 - Red/NIR_1 + Red$	Malinowski <i>et al.</i> (2015)	variation GE-1
	$NDVI_2 = Red - NIR_2/Red + NIR_2$	Wolf (2012)	variation WV-2
NDWI	$NDWI_0 = Green - NIR/Green + NIR$	McFeeters (1996)	original index
	$NDWI_1 = Green + NIR_1/Green - NIR_1$	Malinowski <i>et al.</i> (2015)	variation GE-1
	$NDWI_2 = Coastal - NIR_2/Coastal + NIR_2$	Wolf (2012)	variation WV-2
REI	$REI_0 = NIR_2 - Blue/NIR_2 + Blue * NIR_2$	Shahi <i>et al.</i> (2015)	original index
	$REI_1 = NIR_1 - Blue/NIR_1 + Blue * NIR_1$	-	variation GE-1

Finally, the land use mapping was done through a supervised classification conducted by a decision tree. (rooted on the spectral indices found). It is important to mention that the water with sediments and the impervious units (such as build-up areas and asphalt roads) show a similar spectral behavior, which enables to differentiate them in two classes. The decision trees applied to the WV-2 and GE-1 images and the threshold used for the land use definition are shown in Figures 9 and 10.

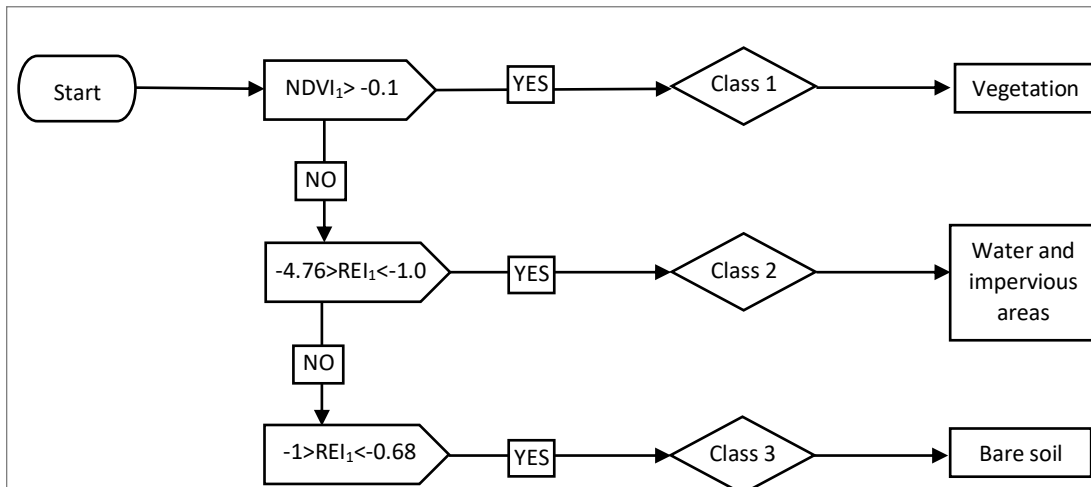


Figure 9. Decision-based tree for land use classification of GE-1 images, with spectral indices and threshold values.

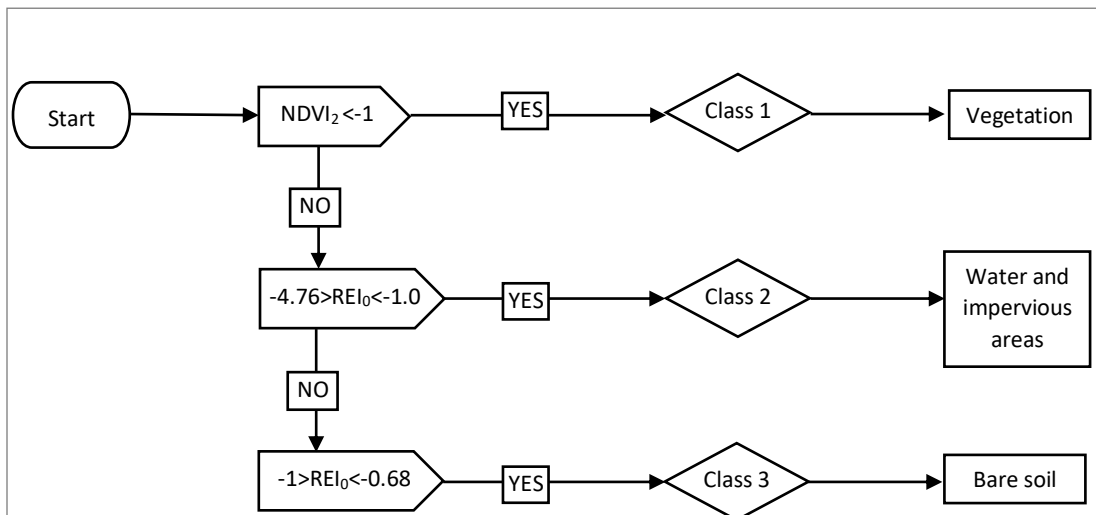


Figure 10. Decision-based tree for land use classification of WV-2 images, with spectral indices and threshold values.

2.2.4. LAND USE CHANGE DETECTION

A visual inspection of the pre-and post-mapping evidenced that land use changes have occurred due to the flash flood episode in the study area. In particular, many vegetation's areas were washed out by the flood while in some cases the water surfaces have increased. Therefore, the core idea to determine the flood extent of Mathew event was to identify the areas where the vegetation and the water surfaces have changed. Since the vegetation could be damaged not only by the flood but by the strong hurricane winds, the change detection was focused on the riverine areas where it was assumed that changes were caused mainly by river floods.

Change Detection classification

The differences between the pre-and post- event scenes were achieved using the Change Detection Workflow tool of ENVI. Firstly, a subtraction of the NDVI and NDWI images was performed, were in principle, a difference was detected in all the pixel values different from a 0. Then, the magnitude of the change (change or no change) and the type of change (increase or decrease) was determined applying a change threshold to the "difference images". The change thresholds were defined after checked the performance of four auto-thresholding methods, from which the Otsu's technique was selected. This is a histogram shape-based method, that it is based on the uses of the zeroth- and the first-order cumulative moments of the histogram for calculating the thresholding values (Harris Geospatial Solutions, 2017). In addition, a clean-up process was computed, using smoothing and aggregation tools to refine the geometry and pattern of the results. As a result, four change detection areas were obtained from the comparison of the images and exported as polygons vector layers (Table 9).

Table 9. NDVI and NDWI change detection areas

	8 oct-2016	9 oct-2016
5 jan-2013	area 3	area 4
1 oct-2016	area 1	area 2

Creating a single flood extent definition.

A single flood extent area was created from the combination of the change detection areas derived in the previous stage. The change detection area 1 and 2 (1th October vs. 8th and 9th October) were used as a main reference of the flood extent the delineation, being complementary in the areas where one on the two images has clouds. The areas 3 and 4 (5th January vs. 8th and 9th October) were used where the previous areas were not spatially covered. The process was conducted in ArcGIS through the Union and Dissolve geoprocessing tool. Finally, some gaps in the polygon were manually filled, to enhance the geometry of the flood extent.

2.3. FLASH FLOOD MODELING

In this study, the open source Limburg Soil Erosion Model (OpenLISEM) was used to simulate the Matthew flood episode over the catchment of Les Cayes. The principles of the model, the input data used in the flood simulations and the calibration procedure performed, are described in the following sections.

2.3.1. LISEM MODEL

OpenLISEM is a physically based numerical model which can simulate hydrological and sedimentological processes (based runoff, flooding and soil erosion modeling) on a catchment scale. It is an event-based model, which means that the simulations are based on short-term rain events (few minutes up to a couple of days). The model has been under continues development since 1996 (see e.g. Baartman *et al.*, 2013; Sanchez-Moreno *et al.*, 2014) and has been used, among other purposes, for investigating the impacts and characteristic of floods (Mhonda, 2013; Jetten and Chavarro, 2016; Nurritasari and Jetten, 2016)

The two main physical processes present in OpenLISEM can be classified into two categories: hydrology and sediments. The subprocesses of both categories and the main model parameters are illustrated in Figure 11. The hydrological processes are shown in red color, the sediment processes in blue and the parameters in dashed red lines.

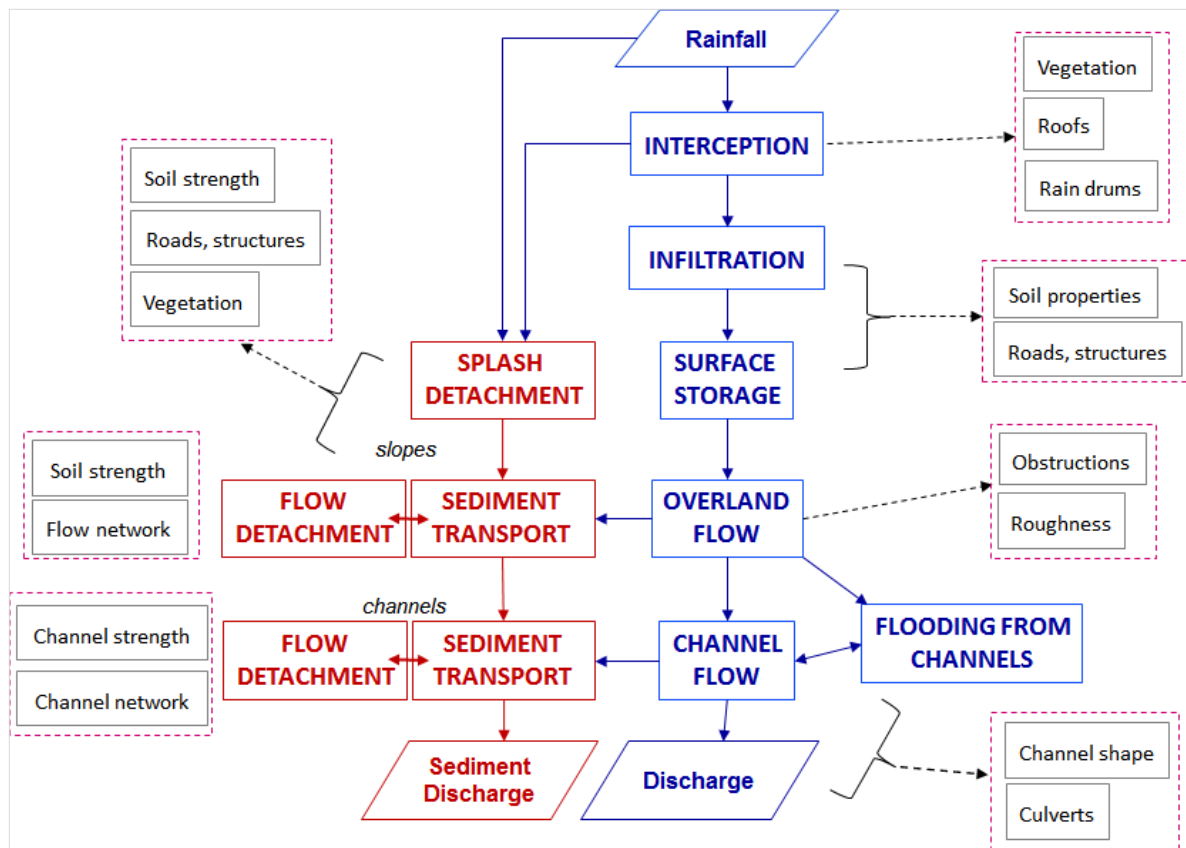


Figure 11. Flowchart of the hydrological and sedimentological processes in OpenLISEM, from (Jetten, 2016)

In this study, only the hydrological processes were used in the modeling (while the sedimentological processes were not simulated). The model hydrology sub-processes are interception, infiltration and surface runoff (overland and channel flow), which main principles are described below.

Interception

The water is intercepted by vegetation, buildings roofs and rain drums in the simulations. The fraction of the rain that falls in a pixel covered by the mentioned surfaces is stored before it reaches the soil layer. In the case of vegetation, the canopy interception is calculated by the equations 8 and 9 (Aston, 1979):

$$Ic = S_{max}(1 - e^{-k \frac{P_{cum}}{S_{max}}}) \quad \text{Equation 8}$$

$$k = 1 - e^{-(co \cdot LAI)} \quad \text{Equation 9}$$

Where,

- Ic : total intercepted storage at a given time (mm).
- S_{max} : maximum canopy storage (mm).
- P_{cum} : total precipitation (mm).
- k : canopy openness parameter.
- co : canopy openness.
- LAI : Leaf Area Index.

For calculating the maximum storage (S_{max}), different equations are included in LISEM, depending on the LAI. The one used in this study was made for Broadleaved Forest, and is given by the Equation 10 (Von Hoyningen-Huene, 1981):

$$S_{max} = 0.2856 * LAI \quad \text{Equation 10}$$

Infiltration

The water that is not intercepted is transported from the surface to the subsurface, according to the hydraulic conductivity and water content of the soil (Jetten and Bout, 2016). The infiltration is simulated by OpenLISEM based on Green and Ampt (1911) and Smith and Parlange (1978) infiltration models. The infiltration rate calculated by the models is given by the empirical Darcy equation (Schmidt, 1996), shown below:

$$\frac{\partial \theta}{\partial t} = -K_s \frac{\partial h}{\partial z} \quad \text{Equation 11}$$

Where,

- θ : soil moisture content ($m^3 m^{-3}$).
- h : hydraulic head (m).
- z : vertical elevation (m).
- K_s : saturated conductivity ($m s^{-1}$).

Surface Runoff

When the rainfall is not intercepted or infiltrated, runoff is generated by the model based on the digital elevation map (DEM). The channels and overland flow are calculated separately, as is illustrated in Figure 12. The main characteristics of the flowing routine, are described below (Jetten and Chavarro, 2016):

The runoff in the channels are simulated with a 1D kinematic wave solution and incorporates the resistant to flow of the bed of the channel (Manning's n). The flow routine is performed over a local drainage network (LDD) and is described by the equations 12 and 13.

$$\frac{dA}{dt} + \frac{dQ}{dx} = q - i \quad \text{Equation 12}$$

$$u = R_2^3 * \frac{\sqrt{S}}{n} \quad \text{Equation 13}$$

Where,

- Q : discharge ($m^3 s^{-1}$).
- A : Cross section of the flow (m^2).
- i : infiltration ($m^3 s^{-1}$).
- q : other sources of water ($m^3 s^{-1}$).
- u : flow velocity ($m ms^{-1}$).
- R : hydraulic radius (m).
- n : Manning's coefficient of the surface ($s m^{-1/3}$).

When the water overflows the channels, it spread outwards (overland flow) using a 2D diffusive wave solution and flowing back into the channels when the level of the water drops. The flowing routine is described by the equations 14.

$$\frac{dA}{dt} + \frac{dQ_x}{dx} + \frac{dQ_y}{dy} = q - i \quad \text{Equation 14}$$

Where,

- Q : discharge ($m^3 s^{-1}$)
- x : component x
- y : component y

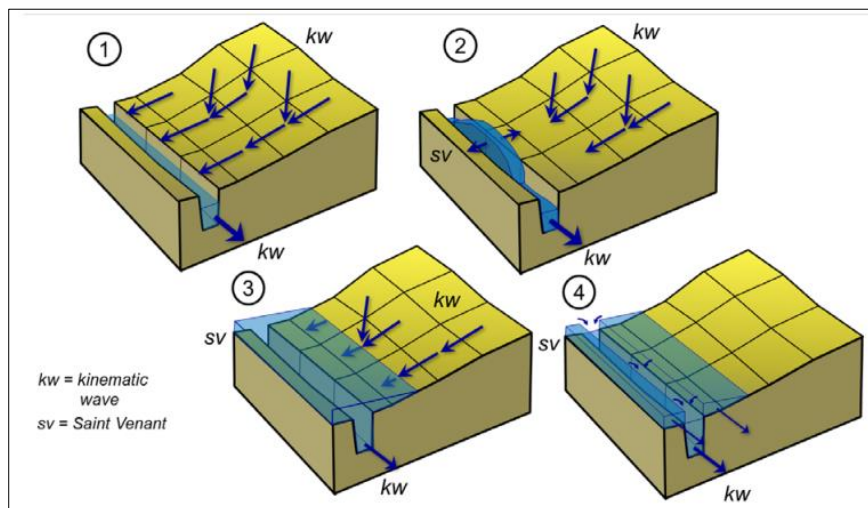


Figure 12. Representation of flow processes in OpenLISEM from (Jetten and Bout, 2016). (1) Channel overflow using a 1D kinematic wave solution. (2) Overflow of the channel. (3) Spread of the channel water using a 2D diffusive wave solution. (4) Overflow water returning to the channel when the water level drops.

2.3.2. MODEL DATASET

OpenLISEM used raster maps as input to determine the hydrological processes that it simulates. In particular, the maps are translated into hydrological and hydraulic parameters related to interception, infiltration, and surface flow resistance.

The maps were created using the geo-information system (GIS) software PC-Raster and were derived from five main input sources, presented in Table 10.

Table 10. List of the main input maps of the study, their sources, and the main procedures performed.

Basic Input map	Created from	Method
Rainfall time serie	IMERG-L: Global Satellite Rain Estimate (SRE) product, grid 0.1 °sec (10.5 m). Variable: half hourly rain intensity (mm/h), source: NASA (2016)	The original rainfall map was scale to a 30.22 meters resolution, using the Inverse Distance Weighted (IDW) interpolation technique, with an exponent 1.
Digital Elevation Model (DEM)	SRTM V.3: Shuttle Radar Topography Mission, 3 rd version), grid 1 arc-sec (30.22 m). Source: USGS (2015).	The DEM was corrected using the filling technique. The corrected channels were burned in the DEM and the main channels bed was decreased in 1 m.
Land use map	Land use and land cover map from the South Department of Haiti, grid 2.5 m. Based on WordView-2 satellite images. Source: CIESIN (2012).	The original land cover map was scale to a 30.22 meters resolution. Hydrological parameters were assigned to the 19 classes, using the study made in Granada by Pratomo (2015) as a reference.
Soil texture Map	SOILGrid250: Global Grid Soil Information Product, grid 250 m. Variable: texture class (USDA). Source: ISRIC (2016).	The original texture map was scale to a 30. 22 meters resolution. The standard soil textures (USDA) class were used to derive soil physical properties with pedo-transfer functions of Saxton et al. (1986).
Building map	Shapefile with buildings of Haiti. Geometry: polygon. Source: Open Street Map	The shapefile was rasterized to a 1 m ² pixel resolution. Then building density was calculated based on the model resolution (30.22 m pixel), through a resampling.
Road map	Shapefile of national roads of Haiti, with 8 classes. Geometry: polyline. Source: Open Street Map	The primary and secondary class roads were assumed to be paved. An average width of 11 m was assigned to primary roads and 5 m to the secondary roads. The polylines were rasterized to a 30.22-pixel size.
Channel maps	SRTM V.3: Shuttle Radar Topography Mission, 3 rd version), grid 1 arc-sec (30.22 m). Source: USGS (2015)	The channels were automatically extracted from the DEM using an LDD and stream order maps. The rivers at the flood plain and mouth of the rivers were manually corrected.

2.3.3. FLASH FLOOD SIMULATION AND CALIBRATION

The flood episode occurred during the pass of Hurricane Matthew was simulated for the catchment of Les Cayes. A time step of 30 seconds was chosen with a total simulation period of 72 hours (4320 minutes), which correspond to 2nd October 19:00 to 5th October 18:30.

The initial moisture content was set as the 85% of the porosity, because the considered rainfall event (Matthew hurricane) happened during the wet season of the study area. In Haiti, the rainy season runs from April to June and intensifies during the cyclonic season (June until end-November), between October and November (Hadden and Manson, 2010).

The flooded extent resulted from the simulations were calibrated against the satellite-detected flooded area delineated in this study. The parameters adjusted to maximize the model agreement with the “observed” flooded extent, are the Manning’s surface roughness coefficient of the channels (channel N) and the channel depth. From all the model parameter, these were chosen because they are directly related with the overflow of the rivers, which is also the processes that were mostly detected in the satellite-based flood extent area (used as a reference in the calibration).

The values were defined by trial and error, however, as a starting reference, the channel Manning’s n the values reported by Carlier d’Odeigne and Soares-Frazão (2016) from the neighboring catchment of Cavaillon were used. In the case of the channel depth, the starting values were created using the operation derived by Jetten (2016) based on Kuriakose *et al.* (2009) study. The method is based on the assumptions that the depth of the soils is shallower in steeper slopes than in flat areas, and that their thickness increases closer to the rivers, while decreases closer to the sea. The values and the combinations of the input parameter used in each calibration are shown in Table 11

Table 11. Input parameter for the model calibration

Run	Channel Manning's n [m ^{-1/3} s]	Channel depth factor	Channel depth [m]
1a	0.03	1	1.20 - 3.24
1b	0.04		
2a	0.03	0.75	0.90 - 2.44
2b	0.04		
3a	0.03	0.4	0.48 - 1.3
3b	0.04		
4a	0.03	0.05	0.06 - 0.162
4b	0.04		

Finally, the accuracy of the flooded simulations in reproducing the satellite-detected flooded extent was quantified using the measure of fit proposed by Horritt (2006), which is shown in the following equation:

$$F = \frac{A}{A + B + C} \quad \text{Equation 15}$$

Where,

- A: Size of the flooded area correctly predicted by the model.
- B: Area predicted as flooded by the model that is actually dry (over-prediction).
- C: Flooded area not predicted by the model (under-prediction)

The values of the fit range between 0 and 1, being 1 a perfect match between the model simulations and the reference area (in this case, the satellite-based detected flood extent)

III. RESULTS: RAINFALL ESTIMATION EVALUATION

This chapter presents the comparison of rain gauge values recorded during the pass of Hurricane Joaquin in the South-West of Haiti, with estimated values from IMERG-L satellite-based product. The detailed temporal evolution of rainfall events is important because the same amount of rainfall falling with different durations can lead to different hydrological processes in a given catchment (e.g. infiltration, soil saturation, runoff, and flood). Therefore, the evaluation was performed based on rain intensities at different time scales.

3.3. EXPLORATORY ANALYSIS OF JOAQUIN RAIN EVENT

Basic statistics from ground and satellite data recorded from 30th September to 3rd October are presented in Table 12. The rain intensities and the cumulative values per hour are shown in Figures 13 and 14, respectively.

Table 12. Summary of rainfall statistics of Joaquin event for observed values from six-gauge stations and corresponding estimated values from IMERG-L product. Observed rain gauge data (G), Estimated rain satellite data (S), Total rainfall (Tot), Maximum accumulated rain (Max), Date of the maximum accumulated rain in 24 hours (Max_{24h})

ID	Tot [mm event ⁻¹]		Max [mm h ⁻¹²]		Max [mm h ⁻²⁴]		Max ₁₂ /Tot [%]		Max ₂₄ /Tot [%]		Date Max _{24h} [date, time]	
	G	S	G	S	G	S	G	S	G	S	G	S
	TIB	33.66	64.93	21.01	25.08	24.03	40.45	62	39	71	62	1 - 2 Oct, 10:00
PPMT	53.09	129.29	39.67	50.27	49.48	94.63	75	39	93	73	1 - 2 Oct, 16:00	1 - 2 Oct, 12:00
RDS	190.24	109.39	117.83	51.34	134.63	82.95	62	47	71	76	1 - 2 Oct, 17:00	1 - 2 Oct, 10:00
SMD	122.15	109.39	85.27	51.34	96.93	82.95	70	47	79	76	1 - 2 Oct, 18:00	1 - 2 Oct, 10:00
LSM	119.62	109.39	83.42	51.34	96.62	82.95	70	47	81	76	1 - 2 Oct, 19:00	1 - 2 Oct, 10:00
USM	95.35	109.39	64.24	51.34	81.89	82.95	67	47	86	76	1 - 2 Oct, 16:00	1 - 2 Oct, 10:00

In terms of the total rainfall amount registered during the event, the ground observations show a spatial variability depending on the station location, where the lower values were recorded at the coastal stations. The values vary from 33.66 mm at Tiburon station (TIB) to 190.2 mm at Ravine du Sud station (RDS). Regarding the satellite estimates, the product highly overestimated the total values at the coastal stations (TIB, PPMT). In the case of the north-east stations (which are compared with the same pixel), RDS is highly underestimated while SMD, LSM, and USM show minors overestimations. These over and underestimations are also evident from the cumulative rainfall plot in Figure 14.

In terms of maximum rainfall accumulation, the ground observations show that depending on the location, 62% to 75% of the total rainfall amount falls in 12 hours and 71% to 93% falls in 24 hours. The maximum concentration of rain in 24 hours occurred at all the stations between the 1st and 2nd October, but at different times. Tiburon station registered the maximum at 10:00, and the others between 16:00 to 19:00. The estimates show lower concentration values: 39% to 47% of the total rainfall amount falls in 12 hours and 62% to 73% in 24 hours. These maximum concentrations occurred earlier than the ground observations. Tiburon station shows a time shift of 11 hours, while the other stations between four and seven hours. These temporal differences are also evident from the rainfall time-series plot in Figure 13.

In summary, the IMERG product detects Joaquin rain event but shows differences in the total rainfall magnitudes, in the maximum rainfall concentrations (accumulated rain per 12 and 24 hours) and in the timings where these maximum amounts of rainfall occurred.

In addition, as can be expected from a rain event produced by a Hurricane, the different magnitudes of rain recorded by the gauge stations reflect the spatial variability of Joaquin in the study area. The fact that four north-east stations (located within the same IMERG pixel) show a non-minor variability evidence that this difference can't be captured by an SRE with a grid of 10.5 km X 10.5 km.

3.4. STATISTICAL EVALUATION

In this section, the evaluation of satellite rain estimates based on six statistical indicators is presented. Specifically, the comparison of the observed and estimated rain intensities during Joaquin event are showed at four times scales (1, 3, 6 and 12 hours).

3.4.1. HOURLY RAIN INTENSITY COMPARISON

In general, the statistics show a low performance of the IMERG-L satellite product estimating rain intensities in mm per hour. The statistical indicators used to quantify the accuracy and error of the SRE are shown in Table 13. In addition, basic statistics from the observed and estimated hourly rain intensities are presented in Table 14.

Table 13. Statistical indicators at hourly rain intensities values


Station	r	ME	MAPE	RMSE	BIAS	E _{FF}	Performance Strong  Weak
	-	[mm hr ⁻¹]	%	[mm hr ⁻¹]	-	-	
TIB	0.13	0.33	242	2.19	1.93	-0.44	
PPMT	0.07	0.79	278	3.45	2.44	-0.99	
RDS	0.12	-0.84	113	5.23	0.58	-0.13	
SMD	0.11	-0.13	132	3.79	0.90	-0.31	
LSM	0.13	-0.11	124	3.57	0.91	-0.33	
USM	0.19	0.15	136	2.95	1.15	-0.51	

Table 14. Summary of rainfall intensities statistics for observed values from six-gauge stations and corresponding estimated values from IMERG-L product. Observed rain gauge data (G), Estimated rain satellite data(S), Sum of the rain intensities (Sum), Arithmetic Mean (Mean), Date of the maximum rain intensity recorded (Max).

	Sum [mm event ⁻¹]		Mean [mm h ⁻¹]		Max [mm h ⁻¹]	
	G	S	G	S	G	S
TIB	33.66	64.93	0.35	0.68	17.20	7.03
PPMT	53.09	129.29	0.55	1.35	21.62	10.65
RDS	190.24	109.39	1.98	1.14	27.81	13.39
SMD	122.15	109.39	1.27	1.14	19.41	13.39
LSM	119.62	109.39	1.25	1.14	17.40	13.39
USM	95.35	109.39	0.99	1.14	18.21	13.39

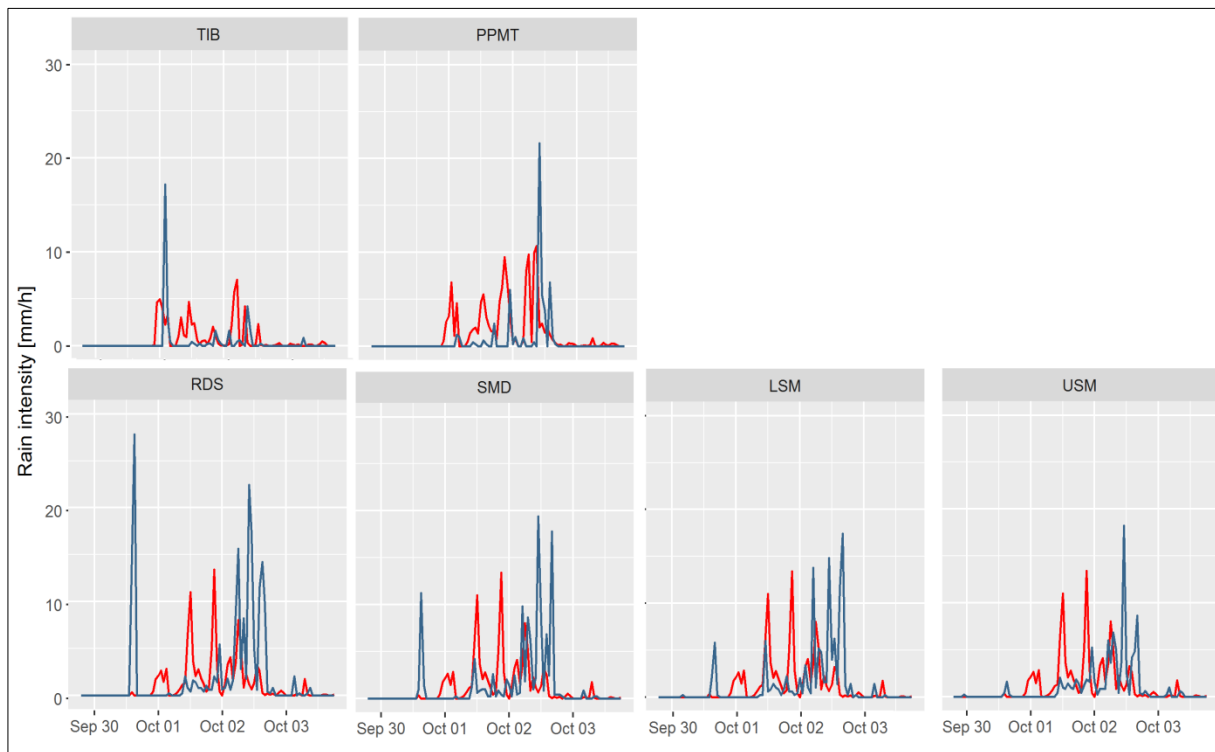


Figure 13. Time-series of hourly rainfall values during the passage of Hurricane Joaquin, per each gauge station. The red line represents the observed data and the blue line the estimated satellite data.

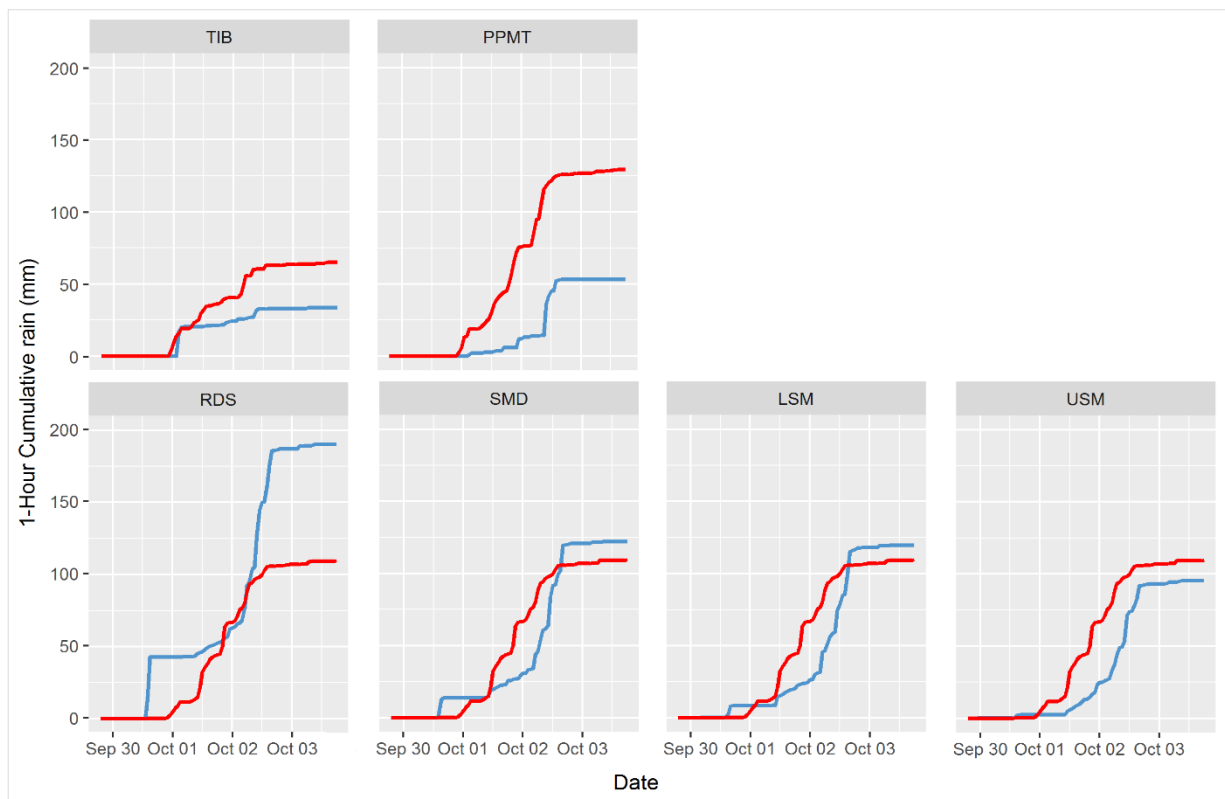


Figure 14. Cumulative rainfall during the passage of Hurricane Joaquin, per each gauge station. The red line represents the observed data and the blue line the estimated satellite data.

The linear correlation coefficient (r) indicates that, in terms of rain amounts, there is a weak relation between the observations and the estimates at all the stations. The efficiency of the product (E_{FF}) is negative at all stations, which signifies that the means of the gauged data are better estimates than the SRE values.

Regarding the average error of the estimates, the RMSE shows magnitudes between 2 to 5 mm/h, while MAPE shows that at all stations the average error is higher than 100%. The ME shows lower magnitudes than the RMSE (-0.84 to 0.79 mm/h). Besides, ME indicates that three of the north-east stations (SMD, LSM, USM) has a good match (values near 0), which doesn't seem to be in line with the RMSE and MAPE. This could be related to the fact that, large positive and negative differences have the risk of cancel each other's, producing ME near 0. In terms of over and underestimation, the ME shows that the coastal (TIB, PPMT) and the USM stations, are overestimated (positive values), while the rest of the north-east stations are underestimated (negative values). The bias of the product shows a reasonable performance (values near 1) at SMD, LSM, and USM stations.

3.4.2. RAIN INTENSITY COMPARISON AT DIFFERENT TIME-SCALES

The comparison of the statistical indicator performance for each time scale (1, 3, 6, 12 hours) is shown in Figures 14, 15, 16 and 17. The statistical indicators values and the basic statistics from the 3, 6 and 12 hours rain intensities data are presented in the appendix.

The linear correlation coefficient (r) indicates that the performance of the satellite product tends to increase when the time scale increases. As is shown in Figure 14, these tendency is clearer at the north-east stations than at the coast, being the lowest values measured at 1-hour rain intensities ($r < 0.2$) and the highest at 12-hours data ($r = 0.29 - 0.48$). In the case of the two coastal stations the correlation increases from 1 hour ($r < 0.13$) to 12 hours evaluation ($r = 0.52- 0.64$), but not linearly during the whole-time scales.

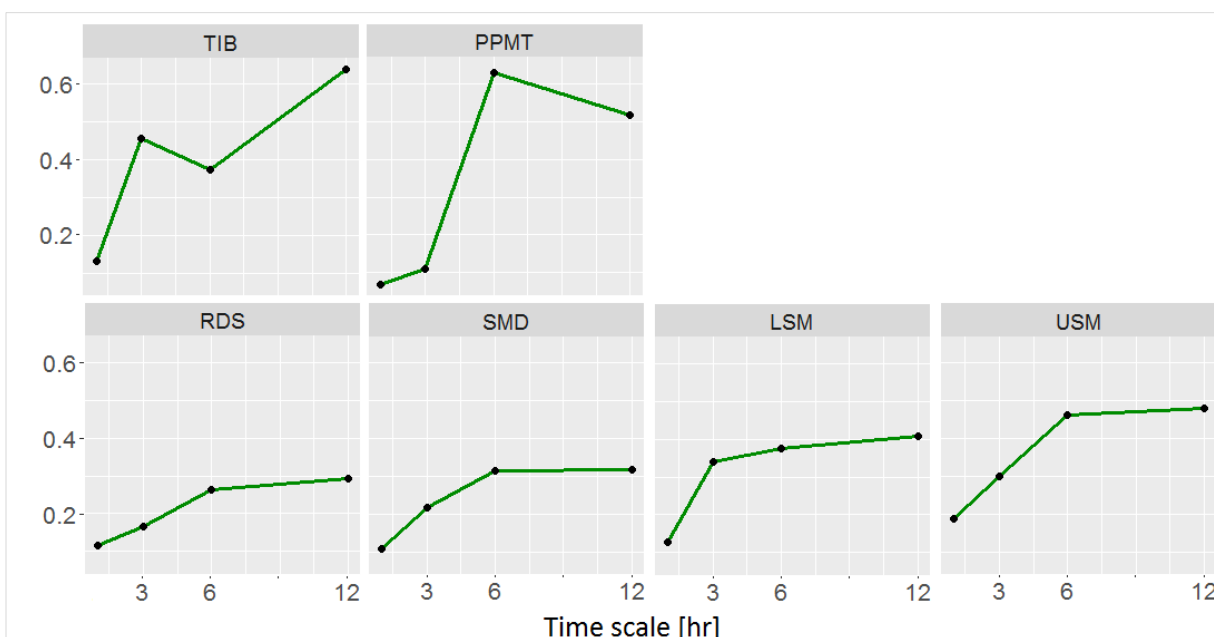


Figure 15. Variation of Linear Coefficient of Correlation (r) at 1, 3, 6 and 12 hours comparison

As is shown in Figure 16 the efficiency of the product (E_{FF}) increases with time scale at the north-east stations, where even two of them shows a good performance (positive values at LSM and USM stations). In contrast, no tendency is observed at the coastal stations.

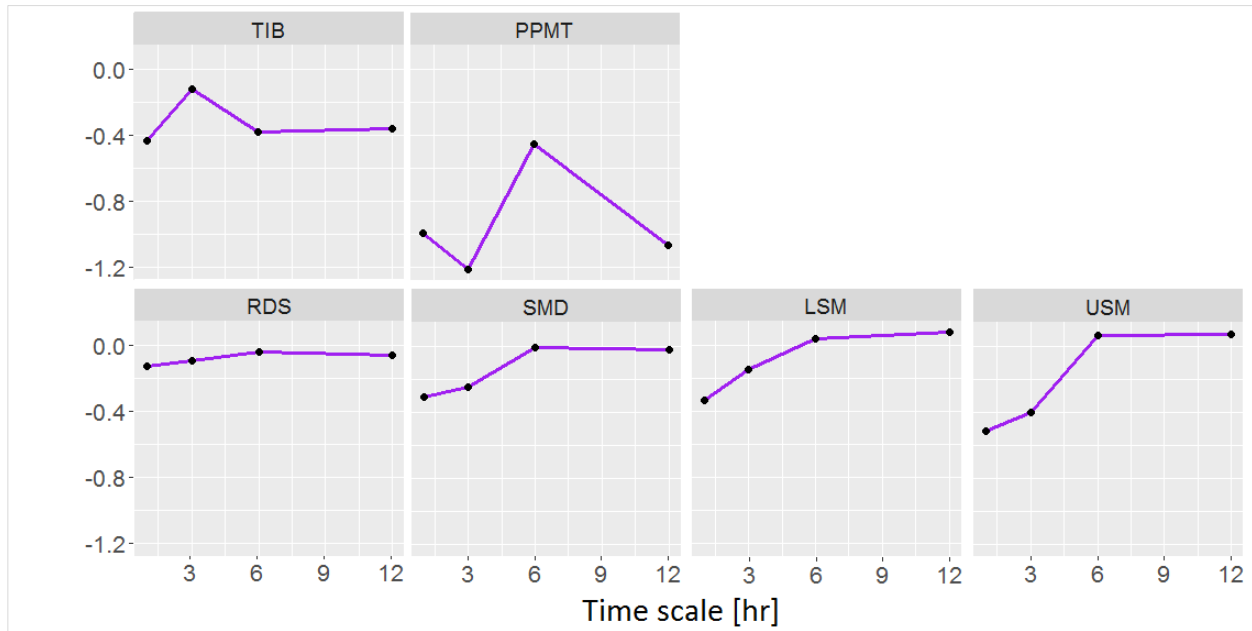


Figure 16. Variation of Efficiency score (Eff) at 1, 3, 6 and 12 hours accumulation comparison.

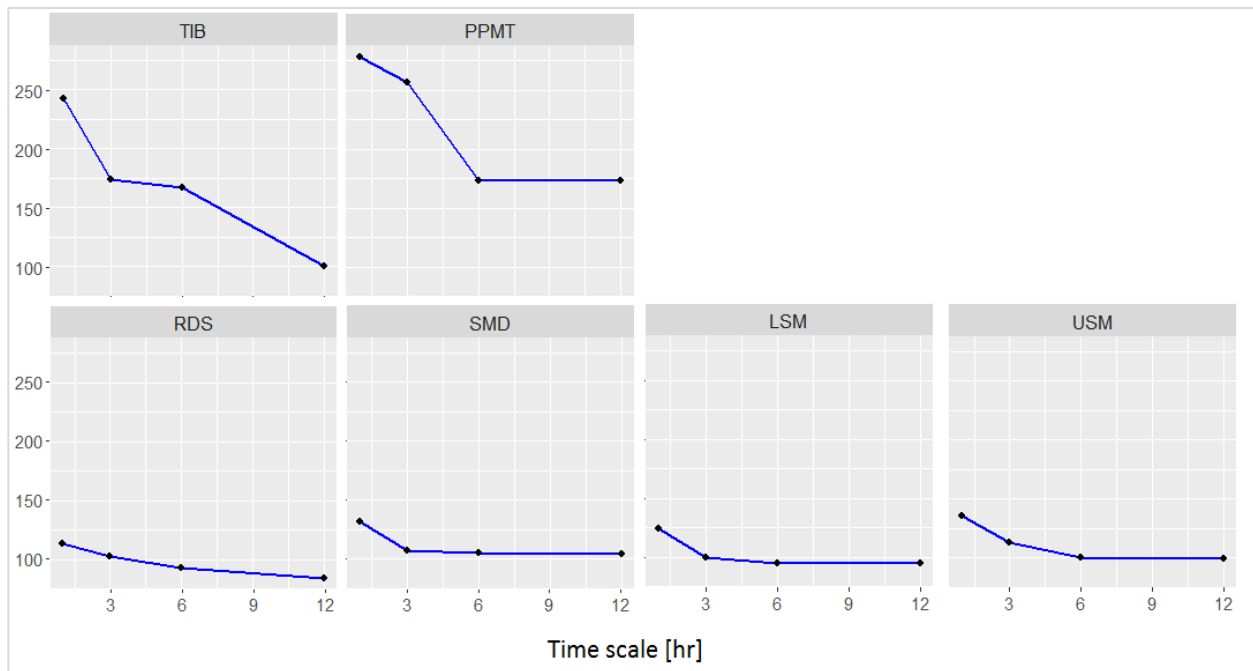


Figure 17. Variation of Mean Absolute Percentage Error (MAPE) at 1, 3, 6 and 12 hours accumulation comparison.

Regarding the average error of the estimates, MAPE shows that the error size decrease when the time scale increase (Figure 17). The reduction of the error from 1 to 12-hours accumulation is important at the

coastal stations (e.g. MAPE at Tiburon station varied from 242% to 100%), while the north-east stations showed a lower variation magnitude. However, the average error size reported by the indicator is high (MAPE > 90%) during all the time-scales at all stations.

ME and RMSE are time scale-dependent indicators, which means that both metrics are sensitive to the number of pair-observations been evaluated (part of the formula denominator, see Table 5). Therefore, cannot be used for comparing the accuracy across time series with different scales as the one used in this study. In other words, as the evaluated rain are accumulations at a different number of hours (during the same period), the time scale has a different number of pair-data, which generates that RMSE and ME increase with the time-scale when it should decrease. The bias of the product shows the same performance across the time scales, due to sum of the estimated values and the sum of the observed values are the same for all the scales.

In summary, the IMERG-L product showed a low skill estimating hourly rain intensities, which tends to increase with the increase of the time scale. The correlation coefficient tends to increase with time scale at all the stations, while the average error (MAPE) decreased. Moreover, the performance of efficiency of the product (E_{FF}) increases with time scale at the north-east stations.

IV. RESULTS: FLOOD EXTENT DELINEATION

This chapter presents the extent of the Matthew flooding episode detected from WorldView-2 and GeoEye-1 imagery in the catchment of Les Cayes.

The satellite-based water extent detected during the 8th and 9th October 2016, is shown with color red in Figures 18 and 19. The size of flooded area is 5.36 km², which according to the land use classification map from CIESIN (2012), inundated a 40% vegetation, 30% agriculture, 25% agroforestry and 5% of urban land covers.

The detected flooded extent represents the 5% of the total area evaluated with the satellite imagery. This total area (illustrated with a yellow line in Figures 18 and 19) represents only the 24% of the whole catchment. However, corresponding to the lower catchment where normally floods impacted and where the city of the Les Cayes is located. The remaining area could not be evaluated, due to the lack of image covering (upper catchment) or because of the presence of clouds (middle catchment).

As is shown in the maps, the flooding extends mostly around the two main rivers of the study area, not reaching the urban zone that lies between these streams. However, an important percentage of the urban area was not take it into account in the assessment, due to the uncertainties of assuming that the detected vegetation changes within the city, were effectively produced by floods and not by the strong winds of the Hurricane. For this reason, the flooding extent presented in this study is expected to be smaller than the real inundation occurred during Mathew event. In consequence, the detected area reflects mostly the riverine inundation of the event and not the plain inundation as the excess of rain or soil saturation. The accuracy of the flooding extent was not tested in this study (due to the lack of ground validation data), but considering the uncertainties is presented in this study as an uncertain flooding map of the event.

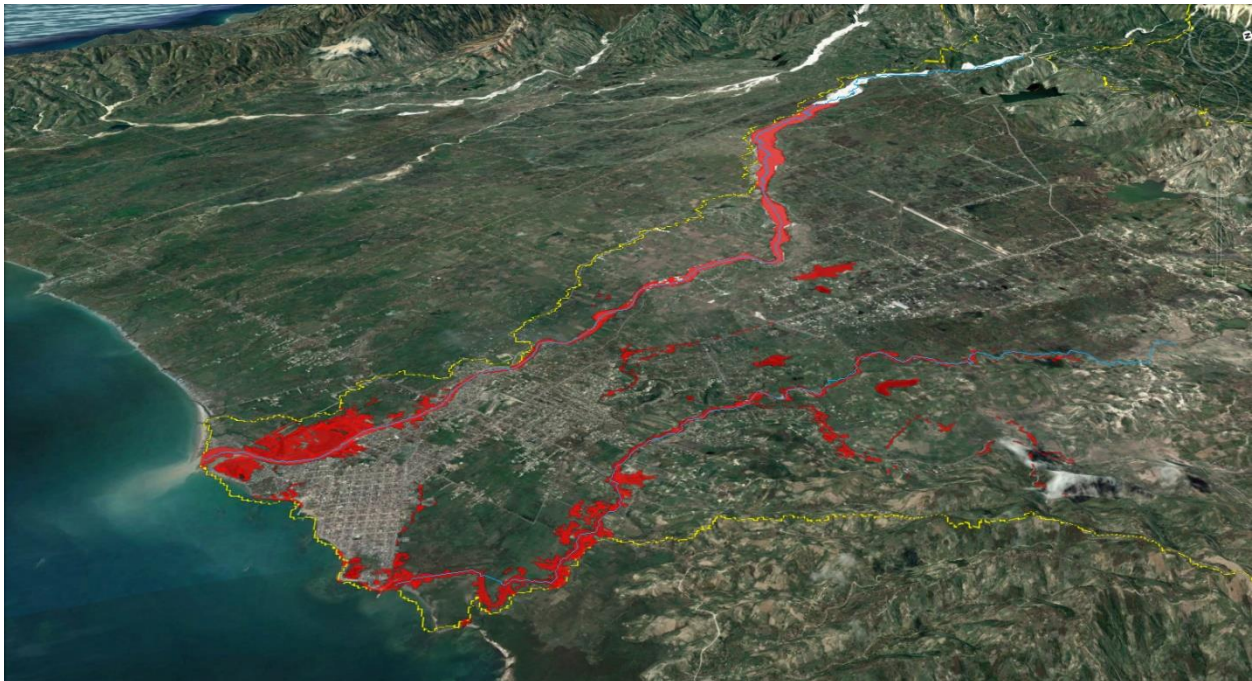


Figure 18. Overview of satellite-detected flooding extent of Matthew flooding episode upon Les Cayes catchment

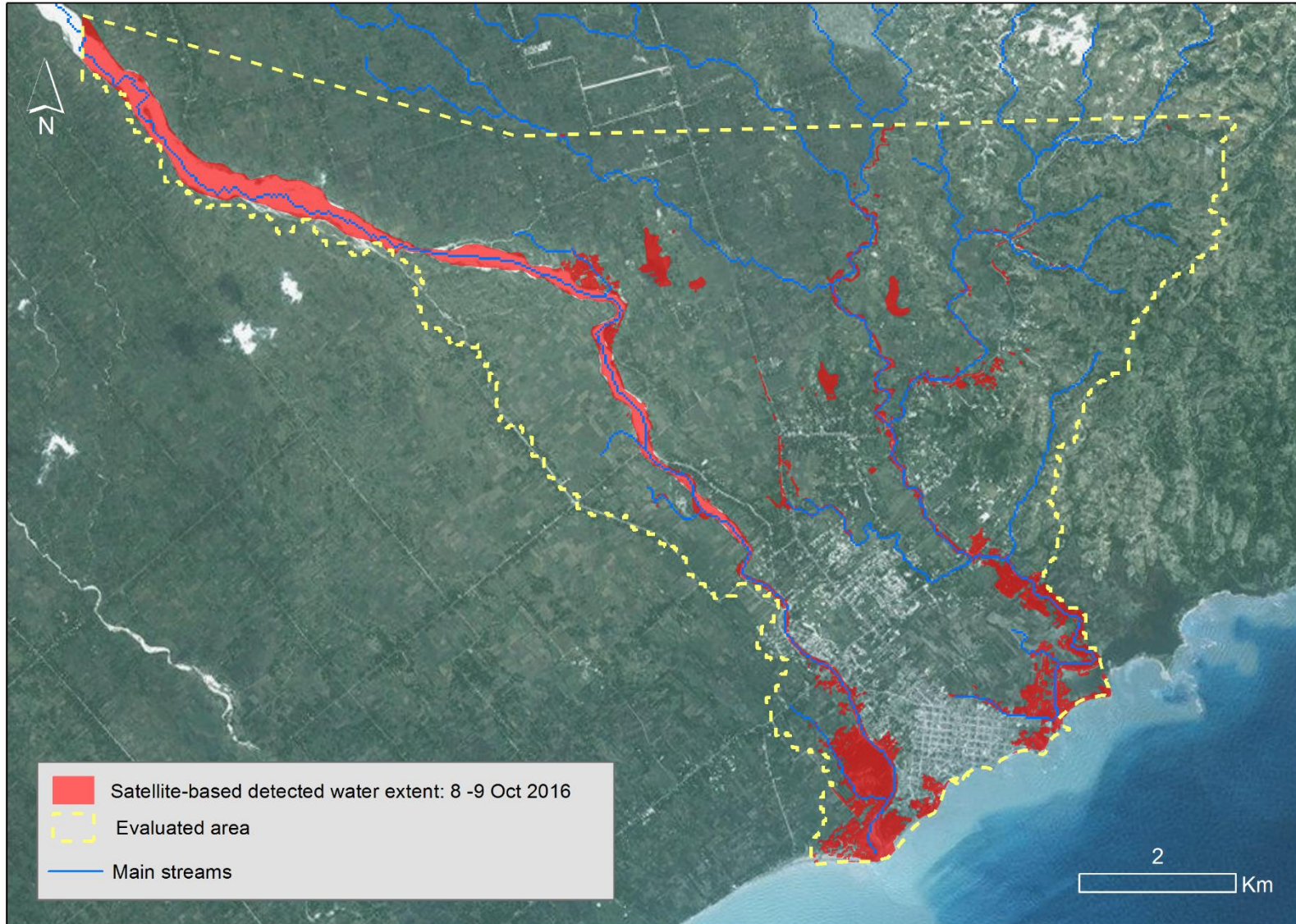


Figure 19. Uncertain satellite-detected flooding extent of Matthew episode upon Les Cayes catchment, in South west Haiti.

V. RESULTS: FLASH FLOOD SIMULATION OF MATTHEW RAIN EVENT

This chapter presents the model simulations of the flood episode occurred in the catchment of Les Cayes, during the pass of Hurricane Matthew. Firstly, the different flooded extent resulted from the model calibration are analyzed. Secondly, the comparison between the simulated flooded areas and the satellite-based detected flooding extent is presented. Finally, the hydrological response of the simulation that better reproduced the flooding event is analyzed.

5.1. CALIBRATION RESULTS

The flooding extent resulted from the calibration of the model and the parametrization used in each of the simulations are shown in Table 15.

Table 15. Input parameter and calibration results of the flood simulations performed in OpenLISEM.

Run	Channel Manning's n	Channel depth		Total simulated flooded extent
	[m ^{-1/3} s]	[factor]	[m]	[km ²]
1a	0.03	1	1.20 - 3.24	15.46
1b	0.04			16.85
2a	0.03	0.75	0.90 - 2.44	17.48
2b	0.04			17.52
3a	0.03	0.4	0.48 - 1.3	21.93
3b	0.04			22.99
4a	0.03	0.05	0.06 - 0.162	24.36
4b	0.04			25.15

The calibration results show that the simulated flooding extent is, as can be expected, very sensitive to the channel depth. The total flooded area of the model increases when the channel depth decrease (because of the decrease of the channel depth factor). The response of the simulated flooded area to four changes in the channel depths are shown in Figure 20.

Regarding the Manning's channel n, the response of total flooded is linear but less sensitive than in the case of the channel depth. The total flooded area of the model increases when the resistance of the channel decrease. However, the variations between the runs performed with Manning's n values of 0.03 and 0.04 are not substantive. The response of the simulated flooded area to the changes in the channel Manning's n is shown in Figure 21.

In sum, the flooded extent of the model is sensitive to the depth of the channel and less reactive to variations in the roughness of the channel (Manning's n). However, additional calibrations are still needed for identifying the optimal parameter values capable of reproducing the reference flooding area of this study.

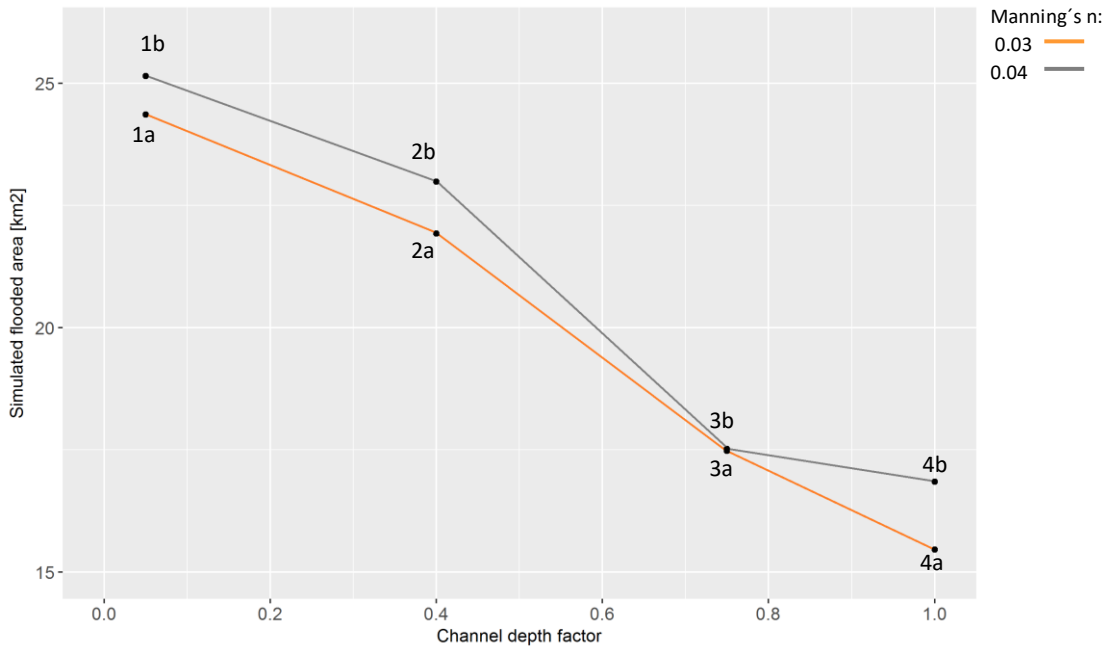


Figure 20. Response of the total flooded area simulated by LISEM to changes in the depth of the channel. The black points represent different runs.

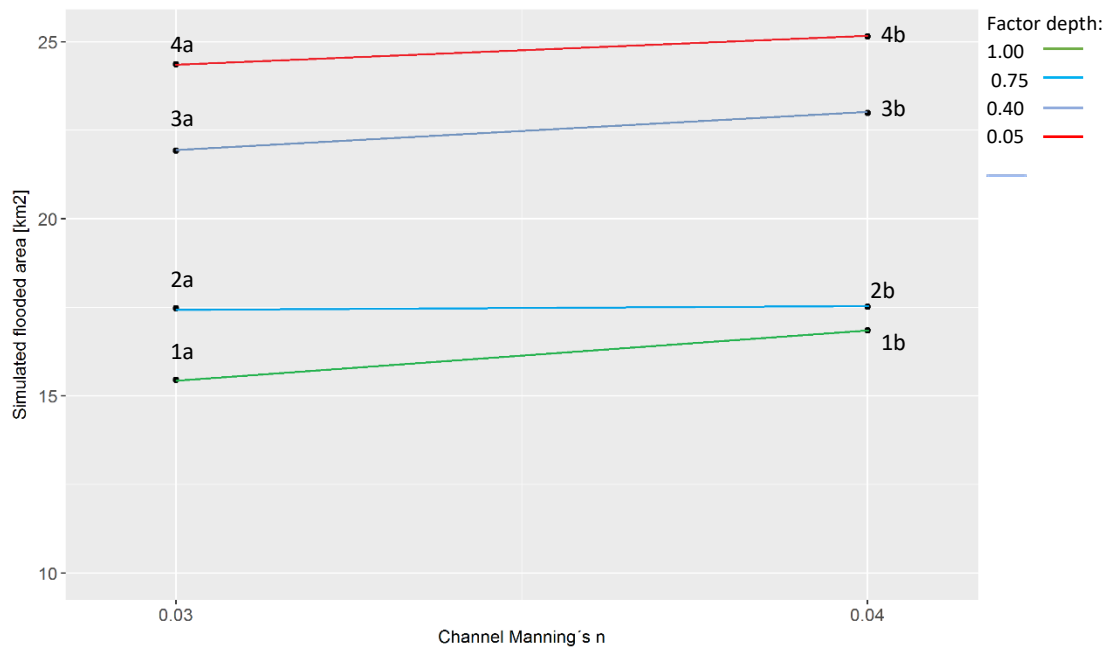


Figure 21. Response of the total flooded area simulated by LISEM to changes in Channel Manning's n. The black points represent different runs.

5.2. SIMULATED AND OBSERVED FLOODED AREA COMPARISON

The performance of the different simulations in reproducing the satellite-detected flooded extent (observed area), are presented in Tables 16 and 17 and can be visualized in Figure 24.

Table 16. Fit of the simulated flood extent with the satellite-detected flood extent.

Run	Corrected predicted area (A)	Over-prediction area (B)	Under-prediction area (C)	Fit of the model (F)	Fit Rank
	[km ²]	[km ²]	[km ²]	(%)	-
1a	1.54	10.24	3.69	9.94	8
1b	3.04	12.10	2.18	17.56	3
2a	3.20	12.26	2.02	18.32	2
2b	3.36	12.29	1.87	19.16	1
3a	3.79	16.71	1.43	17.28	4
3b	3.87	17.24	1.35	17.25	5
4a	4.00	19.14	1.22	16.44	6
4b	4.04	19.93	1.18	16.06	7

Table 17. Comparison of the correct (A) and under (C) prediction areas with the satellite-detected flood extent.

Run	A	A/ Total observed flooded area	C	C/ Total observed flooded area
	[km ²]	(%)	[km ²]	(%)
1a	1.54	29.44	3.69	70.56
1b	3.04	58.28	2.18	41.72
2a	3.20	61.35	2.02	38.65
2b	3.36	64.30	1.87	35.70
3a	3.79	72.61	1.43	27.39
3b	3.87	74.23	1.35	25.77
4a	4.00	76.72	1.22	23.28
4b	4.04	77.39	1.18	22.61

The eight evaluated simulations show a total fit lower than 20% with the satellite-detected area, which in all the runs is given by a high over-prediction area of the model.

All the simulations give a larger flooded extent than the observed flooded area. These high over-predictions showed in Table 16, are also evident from the flooding maps in Figure 25. As can be expected, the runs with the largest over-prediction area (4a, 4b) are the ones with the shallowest channel depth (0.06 m - 0.162 m), independently of the roughness of the channel bed (Manning's n). Conversely, the

runs with the smallest over-prediction area (1a, 1b) are the simulations with the deepest channel depth (1.20 m - 3.24 m).

In terms of the corrected predicted area, as is shown in Table 16, six of the eight runs could reproduce the observed flooding area in 61% to 77 % (2a, 2b, 3a, 3b, 4a, 4b) and show under-predictions between 23% to 39%. The simulations 1a, which has the smallest over-prediction areas, show a corrected predicted area of only 29% and an under-prediction of 71%.

It should be noted that magnitude of the shallowest channel depth used in the runs 4a and 4b, are not likely to be the real situation of the study area channels, but were used to understand the scope of the riverine flooding that could reproduce the model. It was found that when the maximum flooded extent was simulated (using the shallowest channel depth), the floodplain zones that surround the main rivers were flooded. However, two large wooded zones adjacent to the main rivers were not flooded in any of the simulations. As can be easily detected in Figure 22, these zones were flooded by the rivers and the fact that the model underpredicted these areas, shows that the simulations were hindered by the quality of the Digital Elevation Model. It was found, that the two wooded zones were erratically elevated in the SRTM DEM, preventing the flooding in the simulations. Similar errors performed in hydrodynamic modeling of forested floodplains using SRTM, have been described in the literature which is related to the vegetation signal contained within the DEM (Baugh *et al.*, 2013). Even though removing the vegetation signal is recommended to improve the accuracy of the models, this was not tested here and is something to do for future research.

In sum, the run 2b was found to be the simulation that better reproduced the satellite detected flooding area of Matthew event, with a corrected prediction area of 64%, a underprediction area of 36% and a total measure of fit of 19%. The measure of fit of the model used in this study reflects the accuracy of the simulations, considering the corrected predicted area over the sum of the correct, under and over prediction areas. This approach assumes that our satellite-detected flooded area is accurate, which is unlikely to be the case (in fact, as was stated in the previous chapter, it is expected to be smallest than the real inundation). On the above, the low fit values are not surprising, due to it reflect the match of the simulations with an uncertain reference area. Even though urban areas the inundated by the simulations were not considered in the measure of fit computes, it should be considered that the satellite-flooded extent mostly reflects the rivers inundations while the models simulate more runoff processes (e.g. flooding due to soil saturation).

Nevertheless, it was found that the integration that the index makes of the correct, under and over prediction areas, is a useful indicator of how the water extent response to the model parametrization.

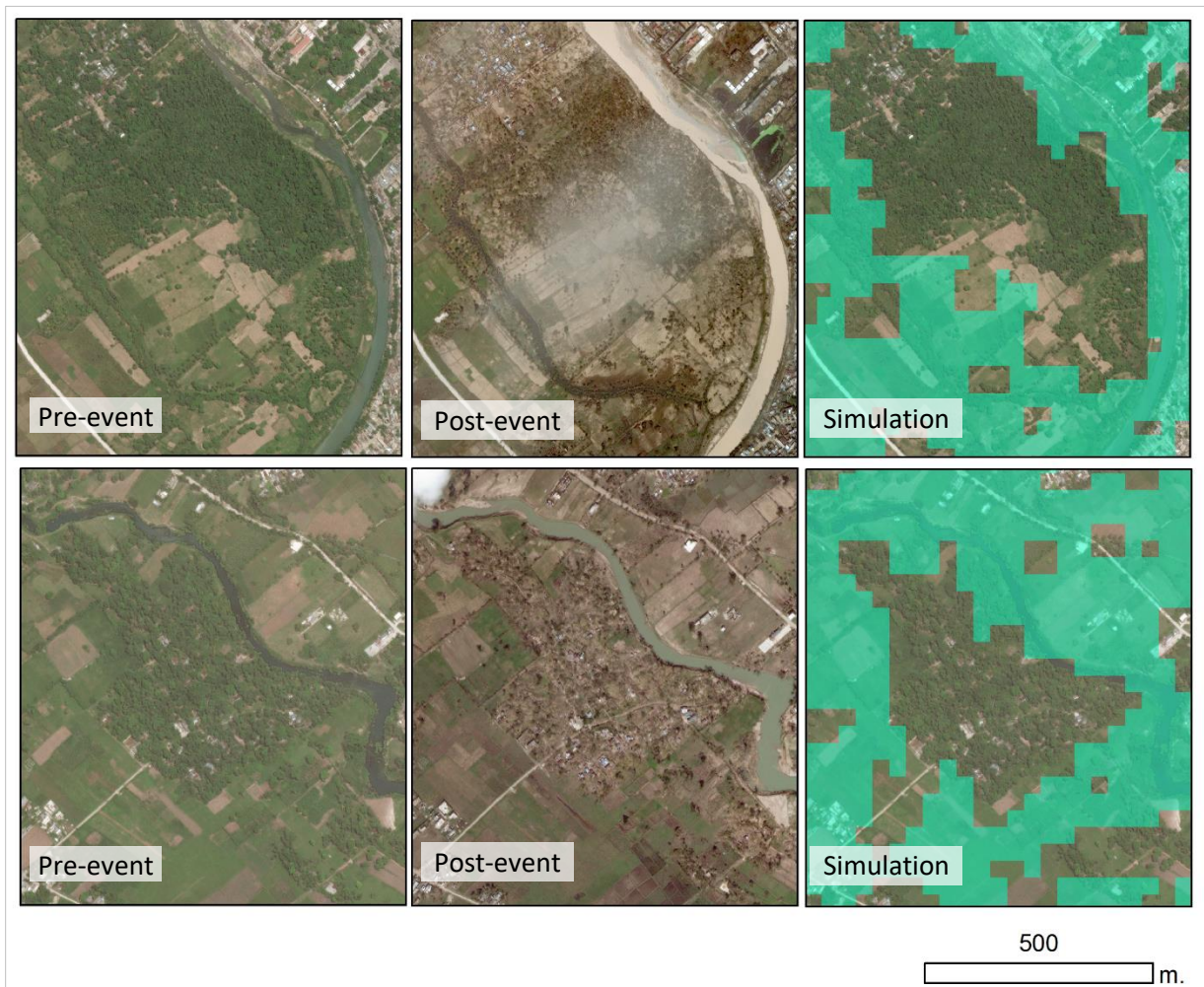


Figure 22. Wooded zones adjacent to the main rivers that were not flooded by the model. The third column images show the simulated flood in green over a pre-event satellite image.

5.3. HYDROLOGICAL RESPONSE AND FLOOD CHARACTERISTICS OF MATTHEW EVENT

This section shows the results of the model simulation that was found to better reproduced the Matthew flooded episode (run 2b) detected by the satellite images. The total average rainfall of the event (estimated from the IMERG-L product) and the simulated total average discharge of the catchment are shown in Table 18. In addition, the hydrograph of the main river outlet point (Ravine du Sud river), is shown in Figure 23. Finally, the main output values of the hydrological simulation are presented in Table 19.

Table 18. Summary of the simulated average discharge and average rainfall of Matthew flooding event, according to the simulation 2b.

Precipitation			Discharge			Peak discharge/ Precipitation
Total	Peak	Peak time	Total	Peak	Peak Time	
<i>mm</i>	<i>mm</i>	<i>min</i>	<i>m3</i>	<i>l/s</i>	<i>min</i>	<i>%</i>
547.88	40.696	2010.50	585,309,82.70	1,195,882.789	2,684	42.45

The catchment response is relatively slow. The discharge starts rising almost while the rainfall peak of the event occurred (time step 2010 .5), which is more than 24 hours after the onset of the rainfall episode. The peak of the discharge occurred 11 hours after the peak of the rainfall (time step 2684), taking more than 24 hours to reach again the base level. The hydrological response suggests that even high rainfall intensities are necessary for inducing the flood, the flood generation is dominated by the saturation of the soil due to the cumulative rainfall over time.

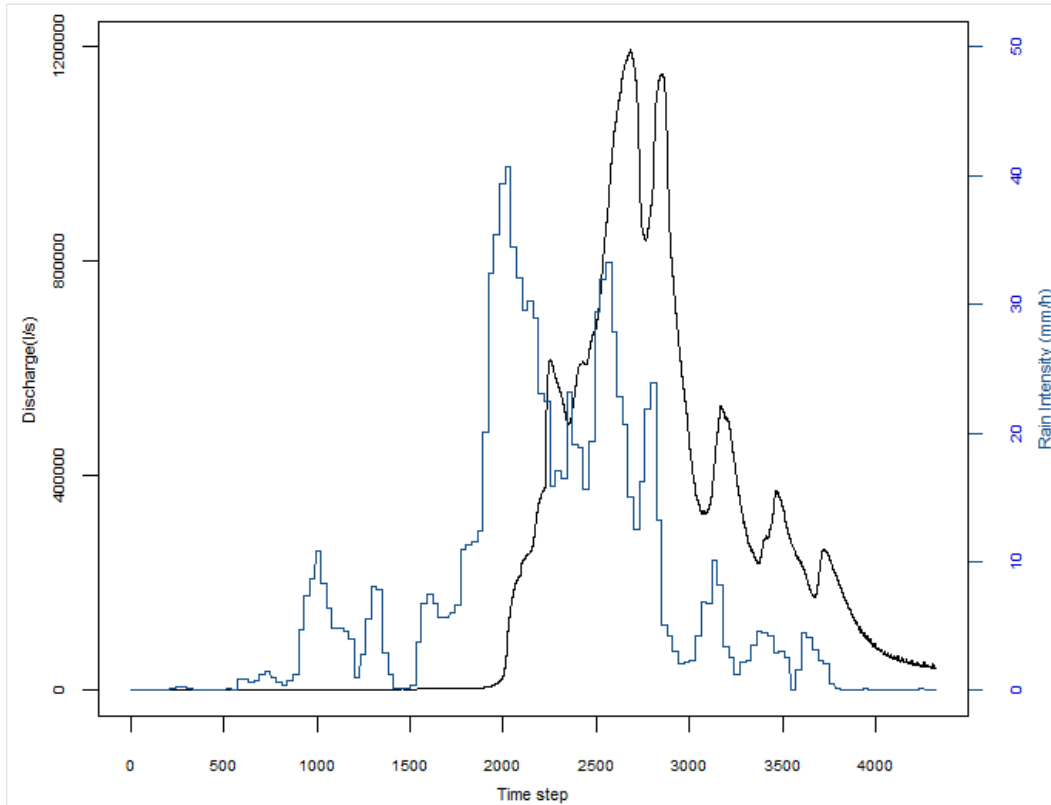


Figure 23. Hydrograph of the flood simulation of Matthew event at Les Cayes Catchment. The black line represents the discharge (l/s) over time simulated by LISEM at the outlet point of the main river. The blue line represents the rainfall (mm h/hour).

Table 19. Simulation results summary

Simulation outcomes			
Model Info	Catchment area [km ²]	268.25	
	Cell size [m]	30.2274	
	Error	2.78207e-11	
Catchment Water Balance		[mm]	%
	Total Precipitation	547.88	100
	Total interception	1.75	0.32
	Total infiltration	292.86	53.45
	Surface storage	0.31	0.06
	Water in overland flow	9.59	1.75
	Water in flood	9.55	1.74
	Water in channels	1.23	0.23
Total outflow (all flows)	232.57	42.45	

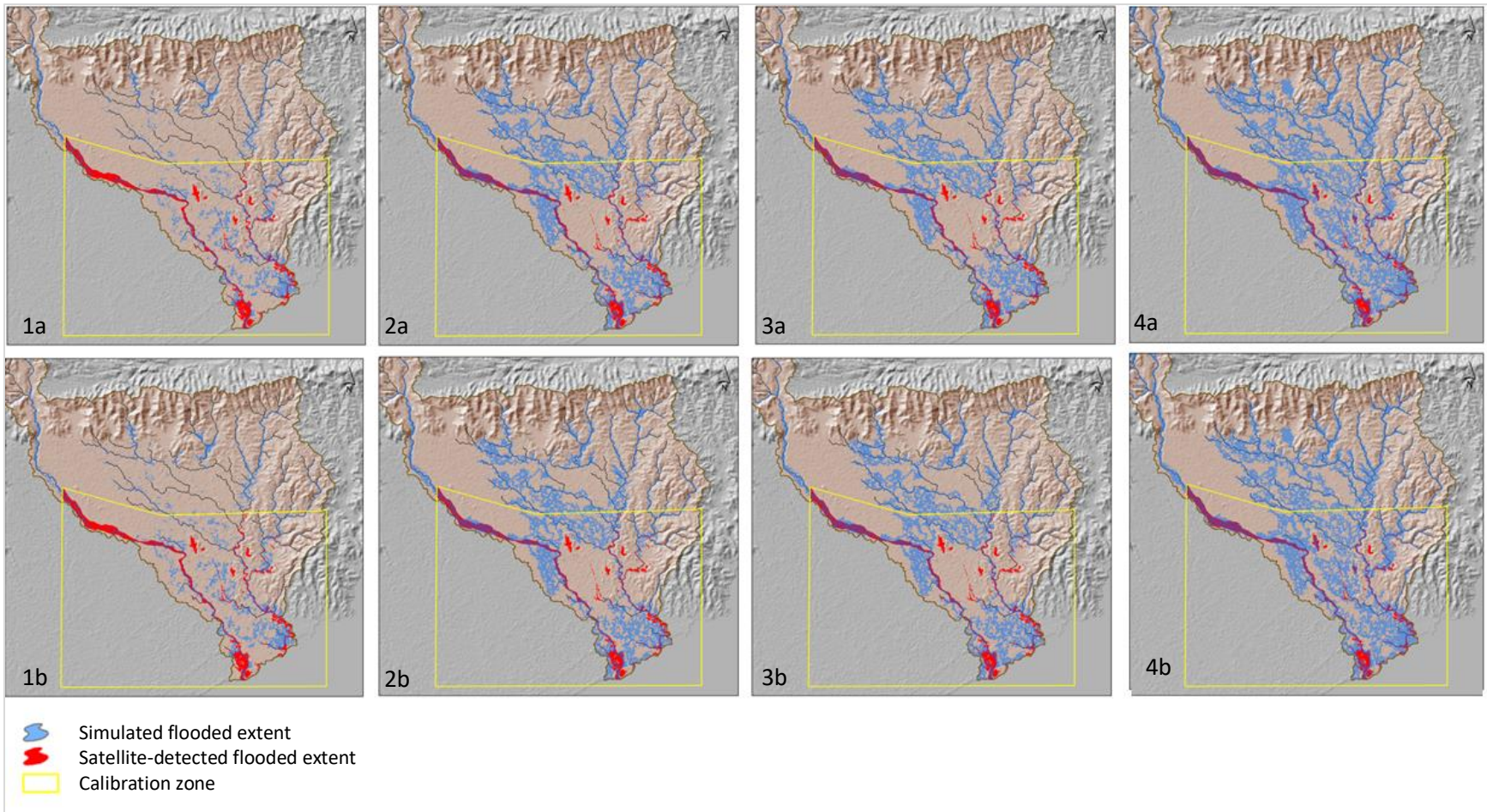


Figure 24. Simulated flooded extent areas of the different runs performed during the calibration process.

VI. DISCUSSION

This chapter presents the discussion of the results of the study. The main findings of the research are placed in perspective according to previous studies. Also, the implications of the method limitations in the results are discussed, and recommendations for methodological improvements are presented.

RAINFALL ESTIMATION EVALUATION

Recent studies have shown that Satellite Rain Estimate (SRE) products are valuable sources of information for estimating heavy precipitations events and droughts, especially in places where traditional ground gauge stations are missing. The performance of the estimations varies depending on the type of SRE used, and on the regional, seasonal and local climate characteristics of the study area, e.g. type of climate, rainy season, influence of topography. However, most of the studies agree with the fact that the accuracy of the estimations improves when the accumulation time scale increases, for instance from daily to monthly, annual or decadal estimations (Gebremichael *et al.*, 2014; Dembélé and Zwart, 2016; Dinku *et al.*, 2017; Zambrano *et al.*, 2017; Zambrano-Bigiarini *et al.*, 2017).

The last generation of Tropical Rainfall Measurement Mission (TRMM) products (TMPA, IMERG) has shown to detect intense rainfall from hurricanes and its eyewall, providing valuable information about the path and development stages of tropical storms (NASA and NOAA, 2003). However, estimating accurate high-resolution precipitation (rain intensity in mm/h) during hurricanes is still a challenging task (Turk *et al.*, 2005; Nourozi *et al.*, 2006), which can be related to the following factors:

- i. Physical characteristics and complexity of the weather phenomenon: hurricanes are large form dynamic systems of spinning air that rotates around a point of low pressure, generating extremely heavy rainfall and intense winds on its passage.
- ii. Rain event duration: the heavy rainfall occurs in a rather brief period which, depending on the intensity of the event, normally concentrates in 12 to 24 hours.
- iii. Availability, spatial distribution, and reliability of rain gauge data: precipitation records during tropical storms are normally scarce, unevenly distributed and prone to errors (e.g. due to high wind speeds).

In this study, IMERG-L showed a low accuracy in estimating hourly rain intensity regarding the Joaquin rain event, but the performance of the product estimation tends to increase when the accumulation time scale increases, which is consistent with the literature. It should be noted that even some stations reported reasonable statistic performances at 12-hour accumulation, the limited ground data used in the analysis enable to have a wider overview of the product accuracy. Given the data scarcity of Haiti, a multi-island evaluation which integrates data from tropical storms recorded in countries like Puerto Rico, Cuba, and the Dominican Republic could contribute to improve the results of the analysis.

SATELLITE DETECTED FLOODING EXTENT BASED ON LAND USE CHANGES

In this study, the inundation area during the Matthew event was detected from multispectral and high-resolution imagery, even though the water surface was not present in the post event satellite images. The proposed method uses the land use changes caused by the flooding to assess the inundation extent of the event. The changes were detected from a comparison of pre-and post-event imagery, based on spectral

indices, images subtraction and decision-based classification with threshold values. However, the method was not exempt from difficulties and yields some limitations which are described in the next paragraphs.

The flooded area was delineated based on changes of only two land covers (vegetation and water), due to the difficulties faced by differentiating the water surfaces land units with impervious covers (built-up areas and asphalt roads) through a spectral analysis. In consequence, the land use changes occurred within the urban area of Les Cayes could not be evaluated in this study.

Since changes in land covers during a hurricane event can be generated not only by floods but also by strong hurricane winds, storm surges, and/or landslides the land cover changes were evaluated mostly around the riverine areas (assuming that these land cover changes were mainly caused by the river overflow). The NDWI index was used to detect the changes in the main rivers and lakes, which increased its wet surface after the event. The NDVI index was used to detect the changes in the vegetation cover that were washed out by the rivers.

Regarding the satellite sensors used in the study, the high spatial resolution and the spectral characteristics of the imagery were found to be suitable to identify the land cover changes with accuracy (according to a visual interpretation). However, the high presence of clouds and haze in the post-event imagery reduced the evaluation area to the lower catchment. Considering the difficulties to find optical clouds-free images during a hurricane, radar imagery has been widely used for detecting flooding because of their all-weather day–night capability (Long *et al.*, 2014; Mason *et al.*, 2014). Moreover, the use of optical sensors has been found unreliable to delineate flooded areas, due to the inability to detect standing water in vegetation (Long *et al.*, 2014; Malinowski *et al.*, 2015).

Given the mentioned difficulties, the satellite-based flood extent presented in this study reflects mostly the riverine inundation which occurred in the lower part of the Les Cayes catchment. Since it is likely that the excess of rain could have generated flooding as well due to soil saturation, it is expected that the real inundation extent is under-estimated by the satellite-detection.

In order to address the aforementioned difficulties in mapping the inundation extent, the following improvements are proposed to be incorporated in the method:

- i) Separate the build-up areas and water surface land covers, using an Object-Based-Image Analysis (OBIA) approach. Considering that the rivers and the buildings present different shape characteristics, OBIA seems to be a promising technique to improve the land use classification and incorporate the urban area in the analysis.
- ii) Use radar imagery. Considering that the proposed method is based on the detection of land cover changes (and not on the detection of the standing water inundation), the use of radar imagery can be a valuable dataset to improve the spatial extension of the performed evaluation.

FLOOD MODELLING CALIBRATION BASED ON SATELLITE DETECTED FLOOD EXTENT

In this study, the inundated area detected from satellite images was compared with that predicted by the model using the measure of fit, showing that the model highly overestimated the observed inundation. However, while the calibration of flood simulations from a single event against ground data (e.g. discharge, flood extent) is conceptually straightforward, the comparison of the model predictions with an uncertain satellite-detected flood extent is more problematic.

VI. CONCLUSION

This chapter presents the conclusions of the study, in the light of the three research questions investigated in this MSc Thesis.

1. How accurate can we assess precipitation of an extreme rain event from satellite-based IMERG products?

The evaluation of the IMERG-L product estimating an extreme rain event upon the South-West of Haiti, showed that the SRE detected the rain event produced by Joaquin hurricane, but shows differences in the total rainfall magnitudes, in the maximum rainfall concentrations (accumulated rain per 12 and 24 hours) and in the timings where these maximum amounts of rain fall occurred. Regarding the total rainfall accumulation of the event, the product highly overestimated the ground values at the coastal stations, while most of the north-east stations reported lower overestimations. In addition, the statistical evaluation shows that the product has a low skill estimating accurate high-resolution precipitation (rain intensity in mm/h) from gauge stations. However, the accuracy of the product estimation tends to increase when the accumulation time scale increases, in accordance with the literature. The linear coefficient correlation (r) between the estimated and the observed data increases at all the evaluated stations, from 1 hour (r between 0.07 – 0.19) to 12 hours accumulations (r between 0.32 and 0.64), but in the case of the coastal stations, not linearly during the whole-time scales. The efficiency score of the product (E_{FF}) increases at the north-east stations, where two of them show a good performance (positive values). In contrast, no tendency was observed at the coastal stations. The Mean Absolute Percentage Error (MAPE) is high during all the time-scales at all stations, but decreases at all stations with the time scale. The reduction of the error from 1 to 12-hours accumulation is important at the coastal stations (around the half), but not that high at the north-east stations.

In sum, IMERG-L product is not accurate estimating high-resolution precipitation (rain intensity in mm/h), having errors in the magnitudes and timings of the rains. However, the total accumulated values show a good match with the observations at the north-east stations, which were the ones that reported the highest accumulated values of the event.

The performed evaluation provides a first insight of the accuracy of IMERG-L product during an extreme rain event derived from a hurricane. However, given the limited number of rain gauge stations analyzed, a further evaluation with a higher number of observations is needed to have a real overview of the accuracy of the product.

2. Can the extent area of the flood episode be detected from satellite images, if the inundation surface is not present in the post-event imagery?

Regarding the second research question, the satellite-based water extent of the Matthew flooding episode was detected from WorldView-2 and GeoEye-1 imagery, upon the lower catchment of Les Cayes.

The method proposed to assess the flooding extent of the event shows that is possible to detect the flooding areas from multispectral and high-resolution optical sensors, based on the land use changes produced by the flooding. However, it presents some limitations which generated that the resulted area reflects mostly the riverine inundation of the event and not the plain inundation due to soil saturation. The main difficulties of the method were the inability of spectrally differentiated the water and the urban areas, and the lack of free-clouds post-event images. In consequence, the flooding delineation was

performed based on the changes of only two land covers (vegetation and water) and the variation within the urban area of Les Cayes could not be evaluated. The total size of the satellite-based flooded area is 5.36 km², but given the mentioned limitations of the method, it expects well underestimated the real inundation of Matthew. The accuracy of the resulted flooding extent was not tested in this study (due to the lack of ground validation data), but given the uncertainties of the method, is presented as an uncertain flooding map of the event.

3. Is the combination of input data and model parametrization capable of simulating the detected flood extent?

With respect to the third research question the combination of input data and model parametrization reproduced the Matthew flood event, but with a high over-estimation. The calibration results show that the response of the simulated flooded extent was very sensitive to changes in the channel depth, and not very reactive to the variations in the roughness of the channel (Manning's channel n). However, further calibrations are still needed for identifying the optimal parameters values to reproduce the detected flooding area. The parametrization of the model revealed that the accuracy of the simulations was reduced by the quality of the input DEM, which erratically elevated wooded zones adjacent to the rivers. According to the literature, this error could be related to the vegetation signal of the SRTM DEM and can be corrected to improve the accuracy of the simulations.

Six of the eight runs could reproduce the observed flooding area in 61% to 77 %, showing under-predictions between 23% to 39%. However, the eight simulations showed a total fit lower than 20% with the satellite-detected area, which in all the runs was given by a high over-prediction area of the model. The resulted lower fit values are not surprising, due to it reflects the match between the flood extent simulations with an uncertain satellite detected flooding area (which it assumes that is accurate).

Given the mentioned points, further calibration of the flood inundation model performed with a corrected and higher resolution DEM, that can cope with uncertainties of the detected flooded area, need to be carried out to simulate with accuracy the Matthew flooding episode at Les Cayes.

VII. REFERENCES

- Aston, A. (1979) 'Rainfall interception by eight small trees', *Journal of Hydrology*, 42(3–4), pp. 383–396. doi: 10.1016/0022-1694(79)90057-X.
- Baartman, J. E. M. *et al.* (2013) 'Exploring the role of rainfall variability and extreme events in long-term landscape development', *Catena*. Elsevier B.V., 109, pp. 25–38. doi: 10.1016/j.catena.2013.05.003.
- Di Baldassarre, G., Schumann, G. and Bates, P. D. (2009) 'A technique for the calibration of hydraulic models using uncertain satellite observations of flood extent', *Journal of Hydrology*. Elsevier B.V., 367(3–4), pp. 276–282. doi: 10.1016/j.jhydrol.2009.01.020.
- Baugh, C. A. *et al.* (2013) 'SRTM vegetation removal and hydrodynamic modeling accuracy', 49(September), pp. 5276–5289. doi: 10.1002/wrcr.20412.
- Berg, R. (2016) 'NATIONAL HURRICANE CENTER TROPICAL CYCLONE REPORT Hurricane Joaquin', (October 2015).
- Bozza, A. *et al.* (2016) 'Potential of remote sensing and open street data for flood mapping in poorly gauged areas: a case study in Gonaives, Haiti', *Applied Geomatics*. Applied Geomatics, 8(2), pp. 117–131. doi: 10.1007/s12518-016-0171-x.
- Brandimarte, L. *et al.* (2009) 'Isla Hispaniola: A trans-boundary flood risk mitigation plan', *Physics and Chemistry of the Earth*. Elsevier Ltd, 34(4–5), pp. 209–218. doi: 10.1016/j.pce.2008.03.002.
- Carlier d'Odeigne, O. and Soares-Frazaõ, S. (2016) 'Determination of bed roughness parameters from field survey: Application to the Cavaillon River, Haïti', pp. 2262–2268.
- CBS NEWS (2016) *Resident of Les Cayes in Haiti: 'It's like a bulldozer just passed by'* - CBS News, CBS Interactive Inc. Available at: <http://www.cbsnews.com/news/hurricane-matthew-resident-of-les-cayes-in-haiti-everything-is-gone/> (Accessed: 28 May 2017).
- Center for International Earth Science Information Network (CIESIN) (2012), Earth Institute at Columbia University. Land Use and Land Cover Map, South Department of Haiti.
- Columbia University (CU) (2017) *Assessing Hydropower Potential in rural Haiti. Hydrological evaluation of three catchments in the South Department*.
- Dembélé, M. and Zwart, S. J. (2016) 'Evaluation and comparison of satellite-based rainfall products in Burkina Faso, West Africa', *International Journal of Remote Sensing*. Taylor & Francis, 37(17), pp. 3995–4014. doi: 10.1080/01431161.2016.1207258.
- Dinku, T. *et al.* (2017) 'Validation of satellite rainfall products over East Africa's complex topography', 1161(June). doi: 10.1080/01431160600954688.
- Dolisca, F. *et al.* (2007) 'Land tenure, population pressure, and deforestation in Haiti: The case of Forêt des Pins Reserve', *Journal of Forest Economics*, 13(4), pp. 277–289. doi: 10.1016/j.jfe.2007.02.006.
- Gebremichael, M. *et al.* (2014) 'Accuracy of satellite rainfall estimates in the Blue Nile Basin: Lowland plain versus highlandmountain', *Water Resources Research*, 50, pp. 8775–8790. doi: 10.1002/2013WR014500.Received.
- Green, W. H. and Ampt, G. A. (1911). Studies on Soil Physics. The Journal of Agricultural Science, 4(01), 1-24.

Harris Geospatial Solutions (2017) *Image Change Tutorial, Documentation Center [Harris Geospatial Docs Center]*. Available at: <https://www.harrisgeospatial.com/docs/ImageChangeTutorial.html> (Accessed: 18 June 2017).

Huffman, G. *et al.* (2013) 'Algorithm Theoretical Basis Document (ATBD) NASA Global Precipitation Measurement (GPM) Integrated Multi-satellitE Retrievals for GPM (IMERG)', *Nasa*, (December), p. 29.

Huffman, G. J., Bolvin, D. T. and Nelkin, E. J. (2015) *Day 1 IMERG Late Run Release Notes*.

INSMET (2016) *Rainfall value during Matthew event in Guantánamo Province*.

ISRIC (2016). SoilGrids250m: Global gridded soil information database. Available at: https://soilgrids.org/#!//?zoom=3&layer=TAXNWRB_250m.

Jetten, V.G. and Bout, B. (2016) *Limburg Soil Erosion Model. Documentation & User Manual*. Enschede.

Jetten, V. G. (2016) *National flood hazard map Saint Lucia*. Faculty of Geoinformation Science and Earth Observation (ITC), University of Twente.

Jetten, V. G. and Chavarro, D. (2016) *Flood modelling for Integrated Watershed Management. Bois d'Orange watershed St Lucia*.

Kuriakose, S.L., Devkota, S., Rossiter, D., Jetten, V.G. (2009). Prediction of soil depth using environmental variables in an anthropogenic landscape, a case study in the Western Ghats of Kerala, India. *Catena* 79(1): 27-38.

Long, S., Fatoyinbo, T. E. and Policelli, F. (2014) 'Flood extent mapping for Namibia using change detection and thresholding with SAR', *Environmental Research Letters Environ. Res. Lett*, 9, pp. 35002–9. doi: 10.1088/1748-9326/9/3/035002.

Malinowski, R. *et al.* (2015) 'Detection and delineation of localized flooding from WorldView-2 multispectral data', *Remote Sensing*, 7(11), pp. 14853–14875. doi: 10.3390/rs71114853.

Mason, D. C. *et al.* (2014) 'Detection of flooded urban areas in high resolution Synthetic Aperture Radar images using double scattering', *International Journal of Applied Earth Observation and Geoinformation*. Elsevier B.V., 28(1), pp. 150–159. doi: 10.1016/j.jag.2013.12.002.

McFeeters, S. K. (1996) 'The use of the Normalized Difference Water Index (NDWI) in the delineation of open water features', *International Journal of Remote Sensing*, 17(7), pp. 1425–1432. doi: 10.1080/01431169608948714.

Mhonda, A. (2013) *Evaluating Flash Flood Risk Reduction Strategies in Built-up Environment in Kampala*. Twente.

NASA and NOAA (2003) 'Case Studies of Transitions from Research to Operations', in *Satellite Observations of the Earth's Environment: Accelerating the Transition of Research to Operations*. National A, pp. 101–138. Available at: <https://www.nap.edu/download/10658#>.

NASA (2016) GPM IMERG-L products, Multi-satellite precipitation estimate with climatological gauge calibration - Late Run (GPM_3IMERGLV03). Available at <https://pmm.nasa.gov/data-access/downloads/gpm>

Nourozi, N., Mahani, S. and Khanbilvardi, R. (2006) 'Validation of Satellite-based Rainfall Estimates for Severe Storms (Hurricanes & Tornados) (2006 - 27Hurricanes_27hurricanes)', in *27th Conference on Hurricanes and Tropical Meteorology*. Monterey. Available at:

https://ams.confex.com/ams/27Hurricanes/techprogram/paper_108722.htm (Accessed: 19 July 2017).

Nurritasari, F. A. and Jetten, V. G. (2016) 'OpenLISEM Flash Flood Modelling Application in Logung Sub-Catchment, Central Java', 47(2), pp. 132–141.

Pacific Disaster Center (2016) *Hurricane Matthew makes landfall in Haiti, continues to impact the Bahamas and U.S., providing weather and hazard related news weather wall. Hazard highlights*. Available at: <http://www.pdc.org/weather/index.php/2016/10/06/hazard-highlights-163/> (Accessed: 20 July 2017).

Pratomo, R. (2015). Flash flood behaviour on a small caribbean island: a comparison of two watersheds on grenada. The Netherlands: MSc thesis, Applied Earth Science-Natural Hazard and DisasterRisk Management. ITC & Utrecht University.

République d'Haïti - (2016) *Huracán Matthew*. Available at: <http://primature.gouv.ht/> (Accessed: 1 December 2016).

REUTERS (2016) *Hurricane Matthew toll in Haiti rises to 1,000, dead buried in mass graves*. Available at: <http://www.reuters.com/article/us-storm-matthew-haiti-idUSKCN12A02W> (Accessed: 1 July 2017).

Rode Kruis Prinses Margriet Fonds (2016) *Building dams in Haiti*. Available at: <https://voorkomderamp.rodekruis.nl/project/bouwen-van-dammen-in-haiti> (Accessed: 19 July 2017).

Sanchez-Moreno, Juan Francisco, Jetten, Victor G, Mannaerts, C M, de Pina Tavares, J. (2014) 'Selecting best mapping strategies for storm runoff modeling in a mountainous semi-arid area Selecting best mapping strategies for storm runoff modeling in a mountainous semi-arid area', *Earth surface processes and landforms*, 39(8), pp. 1030–1048. doi: 10.1002/esp.3501.

Saxton, K. E., Rawls, W. J., Romberger, J.S., Papendick, R.I. (1986). Estimating generalized soil-water characteristics from texture. *Soil Science Society. Am. J.* 50(4): 1031-1036.

Shahi, K. *et al.* (2015) 'A novel spectral index to automatically extract road networks from WorldView-2 satellite imagery', *Egyptian Journal of Remote Sensing and Space Science*. Authority for Remote Sensing and Space Sciences, 18(1), pp. 27–33. doi: 10.1016/j.ejrs.2014.12.003.

Smith, R. E., & Parlange, J. Y. (1978). A parameter-efficient hydrologic infiltration model. *Water Resources Research*, 14(3), 533- 538.

Tucker, C. J. (1979) 'Red and photographic infrared linear combinations for monitoring vegetation', *Remote Sensing of Environment*, 8(2), pp. 127–150. doi: 10.1016/0034-4257(79)90013-0.

Turk, F. *et al.* (2005) 'EVALUATION OF SATELLITE-BASED ESTIMATES OF PRECIPITATION IN THE YUCATAN REGION DURING HURRICANE WILMA', in *27th Conference on Hurricanes and Tropical Meteorology*. Monterey: American Meteorological Society. Available at: https://ams.confex.com/ams/27Hurricanes/techprogram/session_19611.htm.

Updike, T. and Comp, C. (2010) 'Radiometric use of WorldView-2 imagery', *Digitalglobe*, <http://www.digitalglobe.com/downloads/> ..., (November), pp. 1–16. doi: Cited By (since 1996) 9\rExport Date 17 December 2012.

USGS (2006), Shuttle Radar Topography Mission, 1 Arc Second scene SRTM_u03_n18w075 & 074 version 3.0, Global Land Cover Facility, University of Maryland, College Park, Maryland, February 2000.

Von Hoyningen-Huene, J. (1981). Die Interzeption des Niederschlags in landwirtschaftlichen Pflanzenbeständen. Arbeitsbericht Deutscher Verband für Wasserwirtschaft und Kulturbau, DVWK.

Wang, Z. *et al.* (2017) 'Evaluation of the GPM IMERG satellite-based precipitation products and the hydrological utility', *Atmospheric Research*. Elsevier, 196(March), pp. 151–163. doi: 10.1016/j.atmosres.2017.06.020.

Weaver, C., Feaster, T. and Robbins, J. (2016) 'Preliminary Peak Stage and Streamflow Data at Selected Streamgaging Stations in North Carolina and South Carolina for Flooding Following Hurricane Matthew, October 2016.

Wolf, A. F. (2012) 'Using WorldView-2 Vis-NIR multispectral imagery to support land mapping and feature extraction using normalized difference index ratios', p. 83900N–83900N–8. doi: 10.1117/12.917717.

Zambrano-Bigiarini, M. *et al.* (2017) 'Temporal and spatial evaluation of satellite-based rainfall estimates across the complex topographical and climatic gradients of Chile', *Hydrology and Earth System Sciences*, 21(2), pp. 1295–1320. doi: 10.5194/hess-21-1295-2017.

Zambrano, F. *et al.* (2017) 'Evaluating satellite-derived long-term historical precipitation datasets for drought monitoring in Chile', *Atmospheric Research*, 186(November 2016), pp. 26–42. doi: 10.1016/j.atmosres.2016.11.006.

VIII. APPENDIX

RAIN INTENSITY PER 3-HOUR COMPARISON

Table 20. Statistical indicators at 3-hours rain intensities values

Station	r	ME	MAPE	RMSE	BIAS	E _{FF}
	-	[mm event ⁻¹]	%	[mm event ⁻¹]	-	-
TIB	0.46	0.98	174	3.72	1.93	-0.12
PPMT	0.11	2.38	257	8.19	2.44	-1.21
RDS	0.17	-2.53	103	12.33	0.58	-0.09
SMD	0.22	-0.4	106	7.69	0.9	-0.25
LSM	0.34	-0.32	100	6.57	0.91	-0.15
USM	0.3	0.44	113	6.21	1.15	-0.4



RAIN INTENSITY PER 6-HOUR COMPARISON

Table 21. Statistical indicators at 6-hour rain intensities values

Station	r	ME	MAPE	RMSE	BIAS	E _{FF}
	-	[mm event ⁻¹]	%	[mm event ⁻¹]	-	-
TIB	0.37	1.95	167	5.85	1.93	-0.38
PPMT	0.63	4.76	173	9.12	2.44	-0.45
RDS	0.26	-5.05	92	18.44	0.58	-0.04
SMD	0.32	-0.8	105	12.58	0.9	-0.01
LSM	0.38	-0.64	95	11.39	0.91	0.04
USM	0.46	0.88	100	9.33	1.15	0.06



RAIN INTENSITY PER 12-HOUR COMPARISON

Table 22. Statistical indicators at 12-hour rain intensities values

Station	r	ME	MAPE	RMSE	BIAS	E _{FF}
	-	[mm event ⁻¹]	%	[mm event ⁻¹]	-	-
TIB	0.64	3.91	100	7.63	1.93	-0.36
PPMT	0.52	9.52	173	18	2.44	-1.06
RDS	0.29	-10.11	84	32.19	0.58	-0.06
SMD	0.32	-1.59	104	23.8	0.9	-0.03
LSM	0.41	-1.28	95	21.48	0.91	0.08
USM	0.48	1.75	99	17.43	1.15	0.07

